A&A 480, 379–395 (2008)
DOI: 10.1051/0004-6361:20064854

Astronomy & Astrophysics

Chemical abundances in LMC stellar populations

I. The inner disk sample⋆,⋆⋆,⋆⋆⋆

L. Pompéia[1,2], V. Hill[3], M. Spite[3], A. Cole[4,5], F. Primas[6], M. Romaniello[6], L. Pasquini[6], M.-R. Cioni[7], and T. Smecker Hane[8]

[1] IP&D, Universidade do Vale do Paraíba, Av. Shishima Hifumi, 2911, São, José dos Campos, 12244-000 SP, Brazil
[2] Instituto Astronômico e Geofísico (USP), Rua do Matão 1226, Cidade Universitária, 05508-900 São Paulo, Brazil
e-mail: pompeia@univap.br
[3] Observatoire de Paris-Meudon, GEPI and CNRS UMR 8111, 92195 Meudon Cedex, France
e-mail: [Vanessa.Hill;Monique.Spite]@obspm.fr
[4] School of Mathematics and Physics, University of Tasmania, Private Bag 37, Hobart, TAS 7001, Australia
[5] Kapteyn Astronomical Institute, University of Groningen, Postbus 800, 9700 AV Groningen, The Netherlands
e-mail: cole@astro.rug.nl
[6] European Southern Observatory, Karl Schwarschild Str. 2, 85748 Garching b. München, Germany
e-mail: [fprimas;mromanie;lpasquin]@eso.org
[7] Edinburg SUPA, School of Physics, University of Edinburgh, IfA, Blackford Hill, Edinburgh EH9 3HJ, UK
e-mail: mrc@roe.ac.uk
[8] Department of Physics and Astronomy, 4129 Frederick Reines Hall, University of California, Irvine, CA 92697-4575, USA
e-mail: smecker@carina.ps.uci.edu

Received 13 January 2006 / Accepted 13 November 2007

ABSTRACT

Aims. We have used FLAMES (the Fibre Large Array Multi Element Spectrograph) at the VLT-UT2 telescope to obtain spectra of a large sample of red giant stars from the inner disk of the LMC, ∼2 kpc from the center of the galaxy. We investigate the chemical abundances of key elements to understand the star formation and evolution of the LMC disk: heavy and light [*s*-process/Fe] and [α/Fe] give constraints on the time scales of formation of the stellar population. Cu, Na, Sc, and the iron-peak elements are also studied aiming to better understand the build up of the elements of this population and the origin of these elements. We aim to provide a more complete picture of the LMC's evolution by compiling a large sample of field star abundances.
Methods. LTE abundances were derived using line spectrum synthesis or equivalent width analysis. We used OSMARCS model atmospheres and an updated line list.
Results. We find that the alpha-elements Ca, Si, and Ti show lower [X/Fe] ratios than Galactic stars at the same [Fe/H], with most [Ca/Fe] being subsolar. The [O/Fe] and [Mg/Fe] ratios are slightly deficient, with Mg showing some overlap with the Galactic distribution, while Sc and Na follow the underabundant behavior of Ca, with subsolar distributions. For the light *s*-process elements Y and Zr, we find underabundant values compared to their Galactic counterparts. The [La/Fe] ratios are slightly overabundant relative to the galactic pattern showing low scatter, while the [Ba/Fe] are enhanced, with a slight increasing trend for metallicities [Fe/H] > −1 dex. The [heavy-*s*/light-*s*] ratios are high, showing a slow, increasing trend with metallicity. We were surprised to find an offset for three of the iron-peak elements. We found an offset for the [iron-peak/Fe] ratios of Ni, Cr, and Co, with an underabundant pattern and subsolar values, while Vanadium ratios track the solar value. Copper shows very low abundances in our sample for all metallicities, compatible with those of the Galaxy only for the most metal-poor stars. The overall chemical distributions of this LMC sample indicates a slower star formation history relative to that of the solar neighborhood, with a higher contribution from type Ia supernovae relative to type II supernovae.

Key words. stars: abundances – galaxies: Magellanic Clouds – Galaxy: abundances – galaxies: evolution

1. Introduction

During the last decade, the operation of the new class of large telescopes, has led to analysis of the elemental abundances of large samples of individual stars in external galaxies for the first time. Thanks to new optical technologies, objects fainter than supergiant stars, planetary nebulae, or HII regions are now possible targets suitable for extragalactic research, allowing the study of older objects and the exploration of earlier phases of galaxy evolution. The abundance patterns of diverse elements in numerous stars in a galaxy give information on different domains such as the kinematic and chemical evolution, nucleosynthesis channels, the star formation history (SFH), and the initial mass function (IMF) of its stellar population(s).

One of the most interesting extragalactic objects in the study of stellar populations is the Large Magellanic Cloud (LMC),

⋆ Based on observations collected at the VLT UT2 telescope (072.B-0608 and 066.B-0331 programs), Chile.
⋆⋆ Tables 1, 3–8 are only (and Table 2 also) available in electronic form at the CDS via anonymous ftp to cdsarc.u-strasbg.fr (130.79.128.5) or via http://cdsweb.u-strasbg.fr/cgi-bin/qcat?J/A+A/480/379
⋆⋆⋆ Table A.1 is only available in electronic form at http://www.aanda.org

our nearest companion after the Sagittarius dwarf galaxy (that is in the process of merging with the Milky Way). The LMC is an irregular galaxy located within 50 kpc of the Sun, with a kinematically-defined disk, a bar, and a thick disk or flattened halo (e.g. Westerlund 1997). The almost face-on position of its disk, with a tilt of ∼30° relative to the plane of the sky, gives us the precious opportunity to study stars from its different components.

The star formation (SF) and cluster formation histories of this galaxy have been studied for more than three decades (e.g. Butcher 1977; van den Bergh 1979; Olszewski et al. 1996, and references therein; Cioni et al. 2006, and references therein) although a final picture is far from complete (the current status of the research deals with the detailed SF and cluster formation within the different components and regions of this galaxy, e.g. Geha et al. 1998; Smecker-Hane 2002; Subramaniam 2004; Javiel et al. 2005; Cole et al. 2005). The clusters of the LMC show an ancient population with ages >11.5 Gyr, followed by a hiatus when just one single cluster seems to have formed (ESO 121-SC03) (e.g. van den Bergh 1998, and references therein). Some 2−4 Gyr ago, a new formation event was triggered and some other clusters were built (e.g. Da Costa 1991). The SF in the disk field shows a different evolution, with nearly constant rate over most of the history of the LMC (Geha et al. 1998). The SFR appears to have been enhanced some 1−4 Gyr ago, with the timing and amplitude of the "burst" seeming to vary between locations (Holtzman et al. 1999; Olsen et al. 1999). The SFH of the bar field appears to more closely track the cluster formation history, with a strong burst ≈3−6 Gyr ago (Smecker-Hane et al. 2002; Cole et al. 2005). The lack of a field-star age gap means that field star properties can be used to trace the history of the LMC during the 3−11 Gyr cluster age gap (Da Costa 1999; van den Bergh 1999).

The elemental distributions of the LMC stars are still poorly known, because of the paucity of data, but the present picture is changing fast due to new observational programs (e.g. Evans et al. 2005; Dufton et al. 2006; Johnson et al. 2006). We briefly summarize here the results for elemental abundances in the LMC (for a detailed discussion see Hill 2004). The abundance analysis of B stars and HII regions (Garnett 1999; Korn et al. 2002; Rolleston et al. 2002) show a deficient abundance of O, Mg, and Si compared to their solar neighborhood counterparts[1], with mean $\log(\mathrm{X/H}) - \log(\mathrm{X/H})_\odot \sim -0.2$ dex for oxygen, −0.2 dex for magnesium, and −0.4 dex for silicon abundances (this last value is only for the B stars, while HII regions show a much lower value of ∼−0.8 dex), but compatible with galactic supergiant values. Russell & Dopita (1992), Hill et al. (1995), and Luck et al. (1998) studied samples of supergiants in the field of the LMC, and Hill & Spite (1999) derived abundances for supergiants in clusters. They found a similar behavior for the α-elements when compared to the galactc disk values, while for the heavy elements (those with $Z \geq 56$) the abundance ratios are enhanced by a factor of ∼2. Huter et al. (2007) derived C, Mg, O, Si and N abundances for three globular clusters from the LMC, and found an average value 0.3 dex lower than that of the Galactic Clusters for all the analyzed elements, except for N. Red giant branch stars (herafter RGB stars) from the field (Smith et al. 2000, hereafter SM02) and from globular clusters (Hill et al. 2000, 2003, hereafter H00 and H03; Johnson et al. 2006, hereafter JIS06) have also been studied. A general tendency toward low [α/Fe] ratios compared to the stars of the galactic disk with similar metallicities is detected (with the exception of Si and Mg in JIS06), while the same overabundant pattern found for the LMC supergiants has been derived for the heavy-elements. JIS06 inferred the [Y/Fe] ratios and found abundances compatible to the solar value. Sodium abundances are different in field and clusters stars. While SM02 find low [Na/Fe] ratios and [Sc/Fe] ratios close to zero, JIS06 find that [Sc/Fe] and [Na/Fe] ratios are similar to their galactic counterparts. JIS06 have derived the [iron-peak/Fe] abundances to find that Ni, V, and Cu abundances fall below their corresponding galactic values.

An observational project aiming at a full analysis of the elemental abundances of significant samples (∼70−100) of stars from different locations in the LMC has been developed, taking advantage of the FLAMES multiplex facility at the VLT. We obtained spectra from stars in three different regions of the LMC: the inner disk (characterized by a galactocentric radius of $R_C = 2$ kpc); the outer disk (with $R_C = 4$ kpc); and a field near the optical center of the bar. Stars were selected based on kinematics and metallicity data derived from the near-infrared calcium triplet (CaT and CaT metallicities), trying to sample the whole metallicity range of this galaxy as evenly as possible. In the present paper, we focus on a sample of RGB stars on the inner disk region, previosly studied by Smecker-Hane et al. (2002), who derived the ages, metallicities (CaT) and kinematics of this sample. They have identified two kinematical groups in the inner disk field, one with a velocity dispersion of 13 ± 4 km s^{-1}, characterizing a thin disk, and one with velocity dispersion of 34 ± 6 km s^{-1}, probably pertaining to the flattened halo. The metallicities of these two groups are different: the low-dispersion velocity group has metallicities ranging $-0.6 \leq$ [Fe/H] ≤ -0.3 dex, while the high-dispersion velocity component has $-2 \leq$ [Fe/H] ≤ -0.4. The ages derived for this inner disk population has shown that stars have continuously formed during the past ∼1 to 15 Gyr, with a possible enhancement in the SFR some 3 Gyr ago.

As the prototype galaxy of the Magellanic irregular class, to learn the evolutionary history of the LMC is clearly a vital step towards the global understanding of galaxies near the dwarf-giant boundary. Because the Magellanic Clouds have evolved in such close proximity to the Milky Way, their histories have been intimately tied to that of our own galaxy. The ongoing impact of the LMC on the structure and kinematics of the Milky Way is manifest in the warp of the Galactic disk and possibly in the presence of the central bar (e.g., Weinberg 1999), while Bekki & Chiba (2005) have used N-body simulations to show that the LMC could have made a significant contribution to the build up of the Milky Way halo as a result of tidal stripping.

According to models of galaxy formation within a hierarchical CDM scenario (D'Onghia & Lake 2004; Moore et al. 1999), the history of the Milky Way depends strongly on its interactions with its environment. It now seems that the abundance patterns in dwarf spheroidal stars are different from those in Milky Way halo stars (e.g., Shetrone et al. 2001; Tolstoy et al. 2003; Geisler et al. 2005), ruling them out as analogues to the accreting fragments that built the halo up. Study of the LMC takes on added significance in this light, because of the hypothesis by Robertson et al. (2005) that the accretion of LMC-like fragments circumvents this difficulty with the hierarchical accretion scenario. Deeper knowledge of the abundances in the oldest LMC stars therefore has direct bearing on the evolution of our own Galaxy.

In the present paper, we focus on the inner disk region of the LMC, presenting abundance results for iron-peak, heavy and

[1] Taking as the solar value $\log(\mathrm{O/H}) \sim 8.83$ (Grevesse & Sauval 2000).

light *s*-process elements, and α elements for a total of 59 stars. With this detailed information in hand, we aim to shed light on the following questions. (i) What are the chemical abundance patterns of the inner disk of the LMC? (ii) What do these elemental distributions tell us about the formation and evolution of the LMC? (iii) Are they similar to any component of the Milky Way? (iv) Or to the populations of other Local Group galaxies? (v) Based on the elemental distributions, is a merging scenario with LMC debris a likely solution for the Galactic halo formation?

The paper is organized as follows. In Sect. 2 the observations and the reduction procedure are described, the calculation of stellar parameters is presented in Sect. 3, Sect. 4 describes the abundance determination procedures, Sect. 5 reports the results for the abundance ratios and compares them to Milky Way samples, in Sect. 6 we compare our results to those for the dSph galaxies. We discuss the results in Sect. 7, and finally in Sect. 8 give a summary of the work.

2. Sample selection, observations and reductions

To best measure the elemental abundances of the LMC disk and their evolution in time, we selected a field located 1.7° southwest of the LMC bar, in the bar's minor axis direction to ensure a negligible contribution of its stellar populations. An HST color−magnitude diagram study of this field (SMH02) found it to have experienced a rather smooth and continuous history of star formation over the past 13 Gyr, with a possibly increased SFR over the past 2 Gyr. This contrasts with the history of the bar itself, in which significant episodes are seen to have commenced 4−6 Gyr ago (SMH02; see also Holtzman et al. 1999, and references therein). This field has also more recently been the target of a low-resolution spectroscopy campaign (Cole et al. 2000; SMH), using the CaT to derive its metallicity distribution and break the age-metallicity degeneracy inherent to color−magnitude diagram CMD analyses.

We have these infrared CaT metallicities from SMH to select a sample of RGB members of the LMC (based on their radial velocities) distributed uniformly (i.e., with the same number of stars in each metallicity bin) over the whole metallicity range of the LMC disk. In this way, we have been able to sample the lower metallicity bins of the LMC very efficiently. The most metal-poor stars convey essential information on the evolution of the elements of this galaxy, but they are rare, so their number would have been significantly lower if we had selected our sample by picking stars randomly across the RGB. The final sample consists of 67 stars with CaT metallicities ranging from −1.76 to −0.02 dex (including 13 stars with metallicities below −1.0 dex), drawn from the 115-star sample of SMH. In Fig. 1 we show the sample stars overplotted on the color−magnitude diagram of the LMC inner disk region (CTIO photometry from SMH). The sample mean magnitude is $V = 17.25$ mag, bright enough to allow reasonable S/N high-resolution spectra to be acquired.

The observations were made at the VLT Kueyen (UT2) telescope at Paranal during the science verification of FLAMES/GIRAFFE (Pasquini et al. 2000) in January, February, and March 2003, complemented by one night of the Paris Observatory Guaranteed Time Observations in January 2004. In its MEDUSA mode, GIRAFFE is a multiobject spectrograph with 131 fibers of which 67 were used for the present project. The remaining fibers were allocated to targets of other science verification projects in the LMC. The detector is a 2048 × 4096 EEV CCD with 15 μm pixels. We used

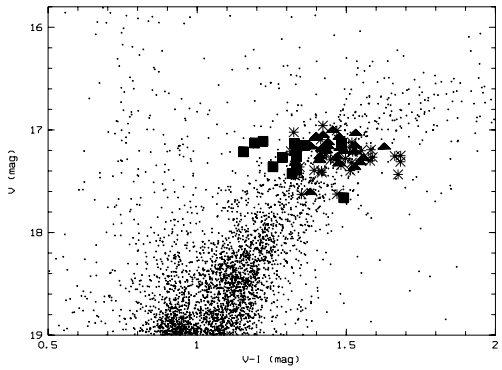

Fig. 1. V vs. $(V - I)$ color−magnitude diagram of the disk region (following SMH02), with our sample stars overplotted: *asterisks* are stars with $[Fe/H]_{CaT} \geq -0.5$ dex, *triangles* $-1.0 \leq [Fe/H]_{CaT} < -0.5$ dex, *squares* $[Fe/H]_{CaT} < -1.0$ dex.

the high-resolution grating of GIRAFFE in three different setups: (i) H14 λ638.3−λ662.6 nm with $R = 28\,800$, (ii) H13 λ612.0−λ640.6 nm with $R = 22\,500$, and (iii) H11 λ559.7−λ584.0 nm with $R = 18\,529$. Exposure times are 6 h for H14 and H13 setups and 7h30 for H11. The setups were chosen to cover the maximum number of key elements such as Fe I and Fe II for spectroscopic calculations of stellar parameters, and α, iron-peak, and *s*-process elements, for the abundance analysis. The average signal-to-noise ratio of the spectra is $S/N \sim 80$ per resolution element.

The data reduction was carried out using the BLDRS (GIRAFFE Base-Line Data Reduction Software `http://girbldrs.sourceforge.net/`) and consists of bias subtraction, localization and extraction of the spectra, wavelength calibration and rebinning. We also used the MIDAS packages for sky subtraction and co-addition of individual exposures.

3. Determination of stellar parameters

3.1. Photometric stellar parameters

A first guess of the stellar parameters was made using photometric data of CTIO (V, I from SHM) and 2MASS (J, H, K). Bolometric magnitudes and effective temperatures were derived from calibrations of Bessell et al. (1998, hereafter BCP). The observed CTIO and 2MASS colors were transformed into the corresponding photometric systems using Fernie (1983, $V - I$ Cousins to Johnson) and Carpenter (2001, K, $V - K$ & $J - K$ 2MASS). Photometric data are given in Table 1, while Table 2 gives the derived effective temperatures ($T_{\rm phot}$) and surface gravities ($\log g_{\rm phot}$). The $T_{\rm phot}$ is derived using the BCP calibration of the deredenned $V - I$ and $V - K$ colors, and the surface gravity is computed using the following relation:

$$\log g_{\rm phot} = 4.44 + \log(M) + 4\log\left(\frac{T_{\rm phot}}{5790}\right) + 0.4(M_{\rm bol} - 4.75)$$

where $M_{\rm bol}$ is computed from the dereddened K magnitude of the star, the bolometric correction BC_K taken from BCP, and the mass of the stars (M) is assumed to be 2 $M_\odot$. A distance modulus based on Hipparcos data and the period-luminosity relations from LMC Cepheids of 18.44±0.05 mag is assumed (Westerlund 1997; Madore & Freedman 1998). Uncertainties of this value stem from the specific subsets of the Cepheids chosen for the comparison (Madore & Freedman 1998). For the reddening, two values were checked: $E(B - V) = 0.03$, which was derived by SMH02 for the sample of the inner disk, using Strömgren photometry; and $E(B - V) = 0.06$, a mean value for the whole

Table 2. Stellar parameters.

Star	$T_{\rm photLow}$	$T_{\rm phot}$	$T_{\rm spec}$	log $g_{\rm phot}$	log $g_{\rm spec}$	[Fe/H]$_{\rm spec}$	[Fe/H]$_{\rm CaT}$	[FeII/H]	$V_{\rm t}$	$R_{\rm v}$
RGB_1055	4066	4118	4266	1.5	0.90	–0.96	–0.87	–0.87	1.2	177
RGB_1105	3921	3965	4100	1.4	0.90	–0.71	–1.15	–0.69	1.6	243
RGB_1118	4102	4154	4204	1.5	1.30	–0.57	–0.25	–0.65	1.8	208
RGB_499	4212	4269	4242	1.4	1.00	–0.85	–0.44	–0.89	2.2	220
RGB_512	4002	4051	4202	1.2	0.80	–0.84	–0.78	–0.89	1.7	247
RGB_522	3971	4016	4101	1.2	1.01	–0.70	–0.37	–0.77	2.0	270
RGB_533	4062	4113	4112	1.2	0.80	–0.75	–0.43	–0.82	2.0	243
RGB_534	4295	4359	4295	1.5	1.20	–1.22	–1.11	–1.12	1.6	246
RGB_546	4055	4107	4185	1.3	0.80	–0.96	–0.91	–0.99	1.7	260
RGB_548	4016	4064	4066	1.2	0.90	–0.74	–0.31	–0.80	2.0	247
RGB_565	3970	4016	4100	1.2	0.70	–0.94	–0.60	–0.96	1.9	242
RGB_576	4064	4117	4190	1.3	0.80	–1.24	–1.03	–1.20	1.6	305
RGB_593	3948	3993	4088	1.2	0.70	–1.15	–0.58	–1.17	1.9	234
RGB_599	4018	4066	4028	1.3	0.80	–0.84	–0.71	–0.81	1.8	241
RGB_601	4071	4123	4101	1.3	1.01	–0.55	–0.77	–0.44	2.0	242
RGB_606	4122	4174	4320	1.4	0.80	–1.74	–1.63	–1.72	1.0	183
RGB_611	3968	4010	3980	1.2	0.70	–0.45	–0.42	–0.55	1.6	244
RGB_614	3756	3967	4107	1.1	0.70	–0.87	–0.71	–0.84	2.2	241
RGB_620	4075	4127	4197	1.4	1.30	–0.61	–0.28	–0.74	2.0	197
RGB_625	3910	3951	4090	1.2	0.70	–0.91	–0.86	–0.91	2.2	242
RGB_629	4099	4150	4229	1.3	0.80	–0.91	–0.97	–0.95	1.7	188
RGB_631	4061	4112	4061	1.3	0.80	–0.64	–0.90	–0.75	1.7	256
RGB_633	4015	4067	4015	1.3	0.90	–0.62	–1.21	–0.55	1.9	194
RGB_640	4089	4141	4280	1.3	0.80	–0.93	–0.82	–0.93	1.9	219
RGB_646	4166	4218	4216	1.4	1.20	–0.72	–0.69	–0.63	1.9	236
RGB_651	4039	4091	4089	1.3	1.10	–0.40	–0.51	–0.46	1.8	247
RGB_655	3948	3988	4048	1.2	0.80	–0.57	–0.66	–0.50	1.8	226
RGB_656	4032	4084	4082	1.3	0.80	–0.71	–0.56	–0.65	2.0	233
RGB_658	3987	4033	4087	1.3	1.10	–0.61	–0.40	–0.57	2.0	231
RGB_664	3840	3881	3900	1.1	0.70	–0.54	–0.58	–0.48	1.9	251
RGB_666	4179	4233	4279	1.4	1.00	–1.02	–1.02	–1.01	1.7	225
RGB_671	3952	3996	4052	1.2	0.90	–0.78	–0.55	–0.70	1.9	249
RGB_672	3866	3906	3956	1.2	0.70	–0.68	–0.38	–0.66	1.9	251
RGB_679	3928	3968	3998	1.2	0.80	–0.63	–0.34	–0.67	2.0	253
RGB_690	3843	3883	3950	1.2	0.90	–0.66	–0.23	–0.70	2.0	296
RGB_699	4458	4531	4488	1.6	1.20	–0.64	–1.15	–0.70	1.4	230
RGB_700	3966	4011	4000	1.3	1.01	–0.60	–0.37	–0.56	2.0	282
RGB_701	3934	3975	4125	1.2	0.70	–0.73	–0.33	–0.65	2.1	257
RGB_705	4182	4237	4202	1.4	1.20	–0.55	–0.72	–0.50	1.6	250
RGB_710	3834	3870	3950	1.1	0.80	–0.75	–0.65	–0.53	1.9	265
RGB_720	3814	4320	4370	1.6	1.40	–0.82	–0.90	–0.85	1.7	200
RGB_728	4102	4153	4252	1.4	0.90	–0.85	–0.80	–0.76	2.1	270
RGB_731	3804	3844	3900	1.1	0.80	–0.48	–0.23	–0.38	1.8	278
RGB_748	3980	4026	4186	1.3	0.90	–0.35	–0.17	–0.32	1.5	223
RGB_752	3915	3956	3915	1.2	1.01	–0.28	–0.08	–0.24	1.8	225
RGB_756	3780	3813	3930	1.1	0.70	–0.82	–0.46	–0.75	2.0	254
RGB_758	4282	4347	4442	1.6	1.20	–0.95	–1.22	–0.92	1.7	257
RGB_766	3971	4016	4156	1.3	0.90	–0.64	–0.46	–0.65	1.9	282
RGB_773	3914	3954	4034	1.2	0.80	–0.87	–0.51	–0.76	2.4	232
RGB_775	4191	4245	4271	1.5	1.01	–0.82	–1.28	–0.82	1.2	241
RGB_776	4118	4170	4178	1.4	1.01	–0.73	–0.75	–0.72	1.7	241
RGB_782	3998	4045	4078	1.3	0.90	–0.57	–0.34	–0.52	1.8	249
RGB_789	3763	3796	3923	1.1	0.60	–0.56	–0.36	–0.58	1.8	245
RGB_793	3982	4029	4169	1.3	0.80	–0.70	–0.53	–0.80	1.9	241
RGB_834	3953	3993	4053	1.3	0.80	–0.86	–0.64	–0.79	2.0	197
RGB_854	4077	4129	4157	1.4	1.20	–0.70	–0.10	–0.82	2.0	313
RGB_855	4065	4117	4257	1.4	1.20	–0.74	–0.02	–0.73	1.9	217
RGB_859	3951	3992	4021	1.3	1.01	–0.64	–0.22	–0.56	1.9	244
RGB_900	4071	4123	4131	1.4	1.01	–0.69	–0.27	–0.64	2.1	276

disk (Bessell 1991). We adopted CaT metallicities from SMH as our initial guesses and reported them in the [Fe/H]$_{\rm CaT}$ column of Table 2.

We derived temperatures from $V-I$, $V-K$, and $J-K$ colors. We found some trends when comparing temperatures from different colors: $T_{\rm eff}(V-I)$ is 65 K hotter than $T_{\rm eff}(V-K)$ in the mean, with σ = 59 K; $T_{\rm eff}(J-K)$ is 21 K hotter than $T_{\rm eff}(V-K)$ and shows a highly dispersed relation, with σ = 118 K (these numbers vary only slightly when choosing a reddening of $E(B-V)$ = 0.06 or 0.03). As initial values of our

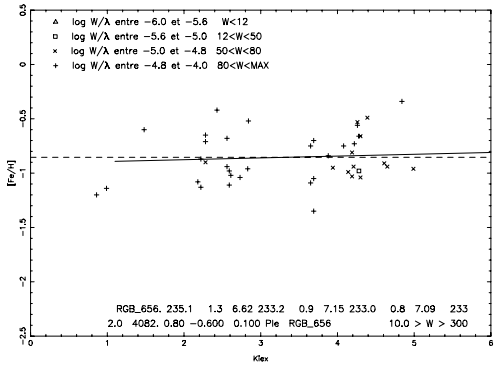

Fig. 2. Example of the temperature calculation for RGB_656: [Fe I/H] vs. $\chi_{\rm exc}$.

stellar temperatures we have chosen to use a weighted mean of the estimates from $V-I$ and $V-K$, omitting the less sensitive $J-K$ color. We assign higher weight to the more temperature-sensitive $(V-K)$, according to the expression

$$T_{\rm eff} = (T_{\rm eff}(V-I) + 2\times T_{\rm eff}(V-K))/3.$$

In Table 2 the inferred temperatures are given for the two values of reddening, $T_{\rm photLow}$ and $T_{\rm phot}$ for $E(B-V) = 0.03$ and 0.06 respectively.

3.2. Spectroscopic parameters

The final stellar parameters used for the abundance determination of the sample stars were derived spectroscopically using abundances derived from the equivalent widths (EW) of iron lines. Although 67 stars were observed, 8 of them have one or two setups with low S/N, compromising the determination of stellar parameters. These stars have not been included in the abundance analysis. Due to low S/N ratios, the H13 setup has not been used for the following stars: RGB_601, RGB_646, RGB_672, RGB_699, RGB_705, RGB_710, RGB_720, RGB_731, RGB_748, RGB_756, RGB_773 and RGB_775; and for RGB_666 the H11 setup has been discarded. We have estimated the stellar parameters as follows: effective temperatures are calculated by requiring no slope in the A(Fe I) vs. $\chi_{\rm exc}$ (excitation potential) plot ($\chi_{\rm exc}$ is the excitation potention of the line); microturbulent velocities, $V_{\rm t}$, are derived demanding that lines of different EW give the same iron abundance, also checking for no slope in the [Fe/H] vs. $\log(W/\lambda)$ plot (iron abundance vs. the reduced EW); and surface gravities are determined by forcing the agreement between Fe I and Fe II iron abundances (within the accuracy of the abundance determination of Fe II). For the temperature and surface gravity ranges covered by our current sample of stars, $T_{\rm eff}$, and $\log g$ determinations are correlated well and the calculation of stellar parameters is made iteratively. In Fig. 2 we show an example of the excitation equilibrium calculation for RGB_656, and in Fig. 3, the [Fe/H] vs. λ with the $\log(W/\lambda)$ check and the [Fe/H] vs. EW are given for RGB_625. The spectroscopic and photometric parameters of all our stars are reported in Table 2, together with the barycentric radial velocities calculated from the spectra.

3.2.1. Equivalent widths, line list, and model atmospheres

The EW of the lines and the radial velocities (RV, in km s^{-1}, reported in Table 2) of the stars are computed using the program

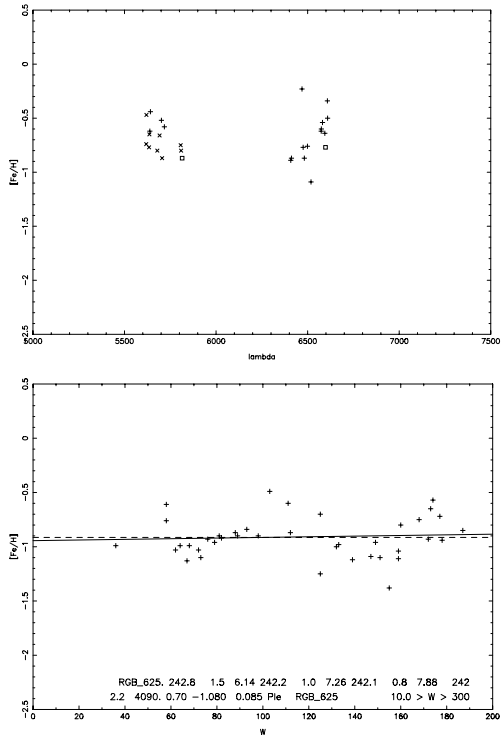

Fig. 3. Examples of microturbulence velocity calculation for RGB_625: [Fe I/H] vs. λ (*upper panel*); and [Fe I/H] vs. EW (*lower panel*). The different values for the reduced EW in the left panel are given with different symbols: 1) squares: $-5.6 \le \log W/\lambda \le -5.0$ and $12 < W < 50$; 2) crosses: $-4.8 \le \log W/\lambda \le -4.0$ and $80 < W < 300$; and 3) times: $-5.0 \le \log W/\lambda \le -4.8$ $50 < W < 80$.

DAOSPEC[2] written by Stetson (Stetson & Pancino, in preparation). The line list and the atomic data were assembled from the literature and the oscillator strengths references are given in Table 4. DAOSPEC has already been used to measure the EW of spectra for different types of stars yielding reliable results (e.g. Pasquini et al. 2004; Barbuy et al. 2006; Sousa et al. 2006). We made a study of the DAOSPEC EW estimations using GIRAFFE spectra. In Appendix A we show a comparison of DAOSPEC EW with those made by hand using the Splot-Iraf task for six of our sample stars. We found very good agreement between the two methods for the analysis of the GIRAFFE spectra within the expected uncertainties.

MARCS 1D plane-parallel atmospheres models (Gustafsson et al. 1975; Plez et al. 1992; Gustafsson et al. 2003) were kindly provided by B. Plez (private communication).

3.2.2. Comparison with UVES analysis

In a previous observing run (066.B-0331), we obtained UVES spectra (in slit mode) for one of our sample stars, RGB_666. UVES is an echelle spectrograph also mounted on the VLT Kueyen telescope with a higher resolving power of $R = 45\,000$ (with a slit of 1″) and a much wider wavelength coverage (in the case of our chosen set-up, 4800–6800 Å), and therefore with a better performance to derive EWs. We used this spectrum to evaluate DAOSPEC performance to derive EW from low-resolution spectra. In Fig. 4, EWs derived with DAOSPEC from UVES spectra from 5800 to 6800 Å are compared to those

[2] The documentation and details about this program can be found in http://cadcwww.dao.nrc.ca/stetson/daospec/.

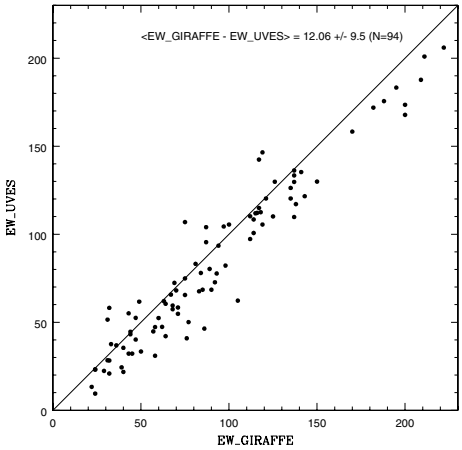

Fig. 4. Comparison between UVES and GIRAFFE spectra analyses for RGB_666.

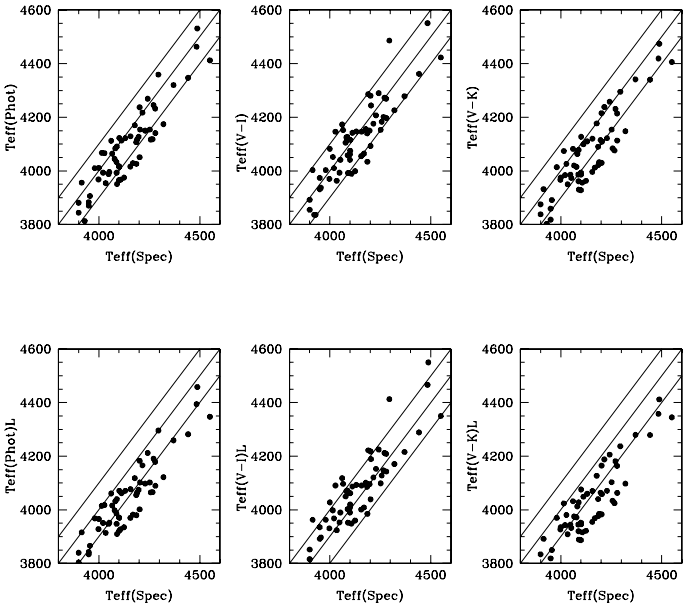

Fig. 5. Comparison between photometric and spectroscopic temperatures (see text). In the bottom plots, photometric temperatures are derived with $E(B-V) = 0.03$ (SMH02), while in the upper plots, photometric temperatures are derived with a higher reddening value, $E(B-V) = 0.06$ (Bessel 1991). Solid lines represent $T_{\rm eff(spec)} = T_{\rm eff(phot)}$ and $T_{\rm eff(spec)} = T_{\rm eff(phot)} \pm 100$ K.

also measured by this program on the GIRAFFE spectra of the same star using the same line list. The top of the plot, the mean differences between analyses are given, together with the dispersion and the number of lines used. Lines of all elements are plotted in this comparison. We can see from this plot that GIRAFFE *EW* are only slightly higher than UVES *EW*. Such a difference is probably due to a better definition of the continuum for the UVES spectra, as well as to the increased blending at the lower resolution of GIRAFFE. Using the *EW* of this figure, we inferred the stellar parameters for UVES to compare the analysis from both spectrographs. We find that the stellar parameters are almost identical to those given for RGB_666 in Table 2, except for $V_{\rm t}$ for which we found $V_{\rm t} = 1.8$ kms^{-1} (a difference of $\Delta V_{\rm t} = +0.1$ km s^{-1}). Comparing the results from the two spectrographs, we have $[{\rm FeI/H}]_{\rm UVES} - [{\rm FeI/H}]_{\rm GIRAFFE} = -0.11$ dex and $[{\rm FeII/H}]_{\rm UVES} - [{\rm FeII/H}]_{\rm GIRAFFE} = 0.00$ dex. Therefore it is possible that a systematic uncertainty of [Fe/H] ~ 0.1 dex may be present in the following abundance analysis, although robust statements on this uncertainty would require better statistics. Let us further note that this 0.1 dex difference is within the errorbar that we quote for our GIRAFFE metallicities.

3.3. Behavior of stellar parameters

We found good agreement between spectroscopic and photometric temperatures. Our spectroscopic temperatures are hotter than photometric temperatures derived using the low reddening value, $T_{\rm photLow}$, by 113 K, with $\sigma = 91$ K, and by 54 K than $T_{\rm phot}$ (higher reddening value) with $\sigma = 64$ K. An interesting result is depicted in Fig. 5 where we compare the spectroscopic temperatures $T_{\rm eff}$(spec) with those derived from colors, $T_{\rm eff}(V-I)$ and $T_{\rm eff}(V-K)$, and from the equation given in Sect. 3.1, $T_{\rm eff}$(phot), for both values of reddening ($E(B-V) = 0.06$ in the upper panels, and $E(B-V) = 0.03$ in the lower panels). This figure shows that photometric temperatures inferred using $E(B-V) = 0.06$ agree much better with spectroscopic temperatures than those derived with the lower $E(B-V)$. Provided that the photometric temperatures and the excitation temperature scale show good agreement, this could indicate that $E(B-V) = 0.06$ is a better reddening value for this region.

On average, spectroscopic surface gravities are lower than the photometric estimates by $\Delta(\log g_{\rm spec} - \log g_{\rm phot}) = -0.38$ dex, as might be expected if NLTE overionization effects are at work (Korn et al. 2003). This systematic effect in $\log g$ corresponds to a 0.2 dex difference between FeI and FeII.

The metallicities that we derive differ on average from those derived from the CaT by $\Delta([{\rm Fe/H}]_{\rm CaT} - [{\rm Fe/H}]_{\rm spec}) = +0.13$ dex with $\sigma = 0.27$ dex. In fact, most of this effect comes from the high-metallicity end of the sample: for $[{\rm Fe/H}]_{\rm CaT} > -0.6$ dex, CaT seems to overestimate the metallicity systematically by 0.27 dex ($\sigma = 0.19$ dex), whereas for the metal-poor end of the sample, there is almost no systematic effect ($\Delta[{\rm Fe/H}]_{\rm CaT} - [{\rm Fe/H}]_{\rm spec}) = -0.04$ dex with $\sigma = 0.24$ dex.

Finally, in Fig. 6, abundance ratios of different species, [Cr/Fe], [Ni/Fe], and [V/Fe], against temperatures are plotted to check the quality of the spectroscopic temperatures. As can be seen from this picture, there is no trend of the abundances of the elements with temperature, which means that our temperatures are well-defined. Our final sample comprises 59 red giant stars within $-1.7 <$ [Fe/H] < -0.30 dex and temperatures ranging from 3900 K to 4500 K.

4. Abundance determination

We have selected a list of lines covering the chosen setups in order to sample the most important elements as much as possible: iron-peak, neutron-capture, and α elements. Abundances are derived from *EW* mesurements for eight elements (in parenthesis the average number of lines used in the analysis): Fe (45), Ni (7), Cr (4), V (11), Si (3), Ca (10), Ti (7) and Na (3). We also derived abundances by using line synthesis for nine elements (in parenthesis the lines used in the synthesis): O ([O I] 6300 Å), Mg I (5711 Å), Co I (5647 Å), Cu I (5782 Å), Sc II (5657 Å), La II (6320 Å), Y II (6435 Å), Ba II (6496 Å), and Zr I (6134 Å). The code used for the abundance analysis was developed by Monique Spite (1967) and has been improved over the years. We note that both model atmospheres and the line synthesis program are in spherical geometry, so errors due to geometry

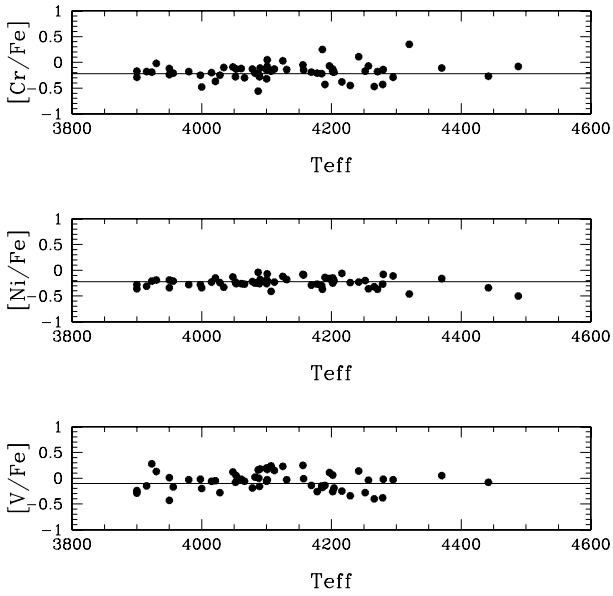

Fig. 6. Abundance ratios against temperatures. *From top to bottom*: [Cr/Fe] vs. $T_{\rm eff}$, [Ni/Fe] vs. $T_{\rm eff}$ and [V/Fe] vs. $T_{\rm eff}$.

inconsistencies are minimized (Heiter & Eriksson 2006). For the synthesis of the [O I] line in 6300.311 Å, we took the blend with Ni I 6300.336 Å (line data from Allende Prieto 2001) into account, but no differences were detected between results with or without such a blend. Hyperfine structures (HFS) have been taken into account for the following elements (the line sources are given in parenthesis): Ba II (Rutten 1978, and the isotopic solar mix following McWilliam 1998), La II (Lawler et al. 2001, with $\log gf$ from Bord et al. 1996), Cu (Biehl 1976), and Co I and Sc II (Prochaska et al. 2000). In Fig. 7 the fitting procedure is shown for the Y I 6435 Å line in RGB_752 and the La II line 6320 Å in RGB_690. Abundances are given relative to solar abundances of Grevesse & Sauval (2000). Atomic lines for the synthesis have been chosen according to the quality of the synthetic fit in the Solar Flux Atlas of Kurucz et al. (1984). The derived abundances are given in Tables 5 to 8.

Errors in the derived abundances have three main sources: the uncertainties in the stellar parameters, the uncertainties in the measurements of the *EW* (or spectrum synthesis fitting), and the uncertainties on the physical data of the lines (mainly $\log gf$). The errors due to stellar parameters uncertainties were chosen as the maximum range each parameter could change not to give unrealistic models atmospheres. The errors $\delta([{\rm X/Fe}])_{\rm model}$ are given in Table 3, assuming the following uncertainties in each of the stellar parameters: $\Delta(T_{\rm eff}) = \pm 100$ K, $\Delta(\log g) = \pm 0.4$ dex, $\Delta(V_{\rm t}) = \pm 0.2$ km s^{-1}, and $\Delta([{\rm Fe/H}]) = \pm 0.15$ dex.

Errors in the *EW* measurement we computed by DAOSPEC during the fitting procedure, then propagated into an abundance uncertainty for each line, and finally combined into an abundance error on the mean abundance for each element ($\delta_{\rm DAOSPEC}$). Errors due to the combined uncertainties on the line data and line measurement are reflected in the abundance dispersion observed for each element, provided that the number of lines is large enough to measure this dispersion in a robust way ($N \geq 3$). We therefore combined these error estimates conservatively as given below:

$$N_{\rm X} < 3 : \delta([{\rm X/H}]) = \delta_{\rm DAOSPEC},$$
$$N_{\rm X} \geq 3 : \delta([{\rm X/H}]) = {\rm Max}\left(\delta_{\rm DAOSPEC}, \frac{\sigma({\rm X})}{\sqrt{N_{\rm X}}}\right) \quad (1)$$

where $N_{\rm X}$ is the number of lines of the element X and σ(X) the dispersion among lines.

These errors were calculated for each element and given in Tables 5 to 7, together with the abundances derived from the *EW*. For elements measured by synthesis spectrum fitting, an error estimate was carried out of the typical abundance change for which two different synthetic spectra (i.e. computed with two slightly different abundances) still satisfactorily fit the same line. On average, these values are the following for each element: δ[Zr/H] = 0.15 dex, δ[Y/H] = 0.15 dex, δ[La/H] = 0.20 dex, δ[Ba/H] = 0.25 dex, δ[Co/H] = 0.10 dex, δ[Cu/H] = 0.20 dex, δ[Sc/H] = 0.10 dex, δ[Mg/H] = 0.15 dex, and δ[O/H] = 0.20 dex. For the error bars reported in our abundance plots (always shown in the lower left corner of Figs. 8–12), we adopted two error sources. The first, caused by stellar parameter uncertainties (leftmost side of the plots), comes directly from Table 3, whereas the second (more to the right side) represents the error associated with the abundance analysis. For those abundances derived from the *EW*, this is the mean error of Tables 5–7, and for those elements with abundances derived from spectrum synthesis, it is the value described earlier on in this section.

5. Abundance distributions and comparison to galactic samples

In Figs. 8 to 12 we depict the elemental distributions for the α-elements, the iron-peak group, Na, Sc, Cu, and *s*-elements for our stars compared to different samples of the Galaxy and the LMC. Our data are represented as dots. The references of the disk are Fulbright (2000, crosses), Reddy et al. (2003, open squares), Allende Prieto et al. (2004, open stars), Prochaska et al. (2000, open triangles), Burris et al. (2000, stars – only for the heavy-elements plots), Johnson & Bolte (2002, open triangles – only for the heavy-elements plots), Simmerer et al. (2004, open hexagons), Nissen & Shuster (1997, asterisks, only stars with low [α/Fe] ratios), Nissen et al. (2000, asterisks – Sc abundances for the low-α stars), and Bensby et al. (2004, open squares – only for the oxygen plot). LMC globular clusters (GC) stars from Hill et al. (2000, hereafter HI00) for O, and Hill (2004, hereafter HI04) for Na, Mg, Ca, and Si are plotted as downward-pointing, open triangles. The LMC GC stars from JIS06 are represented as open diamonds and field LMC red giants of SM02 as open pentagons. Error bars as described in Sect. 4. are shown in the lower left side of the plots.

5.1. Ca, Si, and Ti

In Fig. 8, the elemental distributions for Ca I, Si I, and Ti I are depicted. We find that [Si/Fe] follows roughly the solar ratio with some scatter. The [Ca/Fe] shows a slight decrease with metallicity. Compared to the distribution of the Galactic halo, both Si and Ca mean abundances are deficient by a factor of 3. The Ti I ratios are also underabundant relative to Galactic disk and Galactic halo samples, and agree very well with the results of SM02, who derived Ti abundances from neutral lines for a sample of red giants from LMC disk. There is a hint of a decreasing trend of Ti abundances for higher metallicity stars, especially when SM02 datapoints are taken into account with our sample. Compared to the LMC GC of H04, we find that the star of our sample with metallicity similar to those of those of Hill et al. (2004) also has a similar [Ca/Fe] ratio. The JIS06 sample of LMC GC stars seems to overlap our [Ca/Fe] and [Ti/Fe] distributions, while their [Si/Fe] ratios are enhanced.

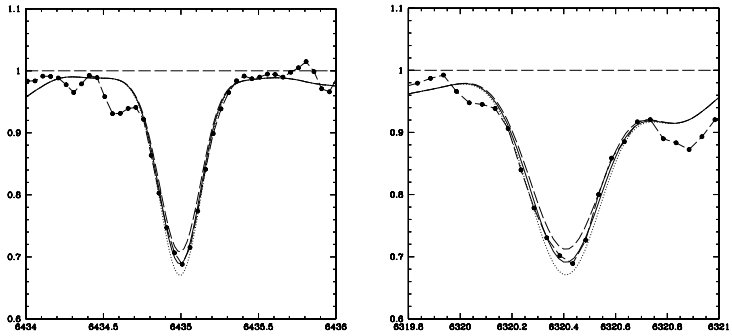

Fig. 7. Example of the line synthesis procedure for the Y I and La II lines: *left panel*: Y I λ6435Å line fitting for RGB_752; *right panel*: La II Å 6320 line fitting for RGB_690. The black circles depict the observed spectra and the lines are the synthetic spectra. Abundances of the synthetic spectra are [Y/Fe] = −0.55 (dashed line), −0.45 (continuous line – best fit), −0.25 (dotted line), [La/Fe] = 0.56 (dashed line), 0.66 (continuous line – best fit), and 0.76 (dotted line).

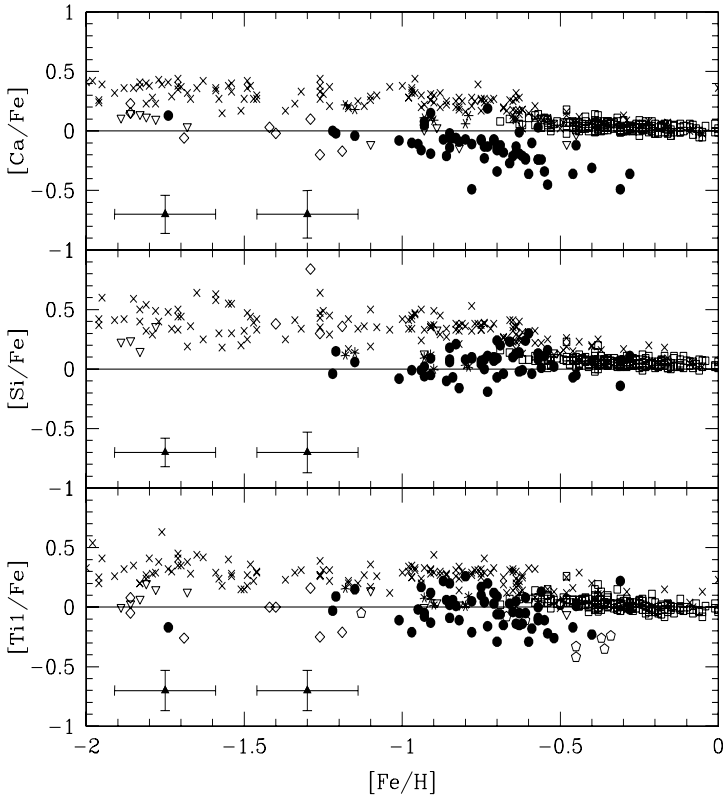

Fig. 8. Abundance distributions for the inner disk LMC stars: [α/Fe] vs. [Fe/H] (dots). LMC samples are depicted with polygons (downward-pointing triangles – Hill et al. 2000; pentagons – Smith et al. 2002; diamonds – Johnson et al. 2006); and the remaining symbols are data for the galactic stars (crosses – Fulbright 2000; open squares – Reddy et al. 2003; asterisks – Nissen & Schuster 1997). Error bars depict a) leftmost side of the plots – errors due to stellar parameter uncertainties (Table 3), and b) more to the right side – errors associated with the abundance analysis – for those derived from the *EW*, is the mean error of Tables 5−7; for those elements with abundances derived from spectrum synthesis, the value is described in Sect. 4.

A very interesting result emerges when comparing our data with those of Nissen & Shuster (1997, hereafter NS97, asterisks). NS97 discovered a sample of stars from the Galactic halo with abnormal abundances: low [α/Fe], [Na/Fe], and [Ni/Fe] ratios compared to "standard" halo stars. Such chemically peculiar or "low-α" halo stars play an important role in elucidating the possible merging history of the Galactic halo. Because of their chemical properties, they indicate that this group has formed in another stellar system that evolve separately and has been captured or ejected to the halo. Comparing our LMC distribution to the low-α stars, we have found that NS97 stars show a slightly enhanced mean α abundance compared to our LMC stars.

Silicom, Ca and Ti are predicted to be produced in intermediate mass type II SNe (SNe II) with a smaller contribution from type Ia SNe (SNe Ia) (e.g. Tsujiomoto et al. 1995; Thielemann et al. 2002), while Fe is mostly produced by SNe Ia (e.g. Thielemann et al. 2001; Iwamoto et al. 1999). The low [α/Fe] ratios observed indicate that SNe Ia has contributed more to the ISM content in the past than the SNe II.

5.2. Mg, O, Na and Sc

In Fig. 9, abundance ratios are given for O, Mg, Sc, and Na. Nucleosynthetic predictions attribute the main source of O, Mg, and Na to high-mass stars, with $M > 25\ M_{\odot}$, which explode as SNe II (Woosley & Weaver 1995, hereafter WW95), with Na production controlled by the neutron excess. Although WW95 attribute the origin of Sc to SNe II, the main source of Sc production is still unclear (e.g. McWilliam 1997; Nissen et al. 2000).

As can be seen in the upper panel of Fig. 9, oxygen ratios fall in the lower envelope of the Galactic halo and disk distributions. For higher metallicities, it shows a faster decline with metallicity compared to stars from the Galactic disk. In the second plot we see that the [Mg/Fe] ratios for the LMC Inner Disk overlap those

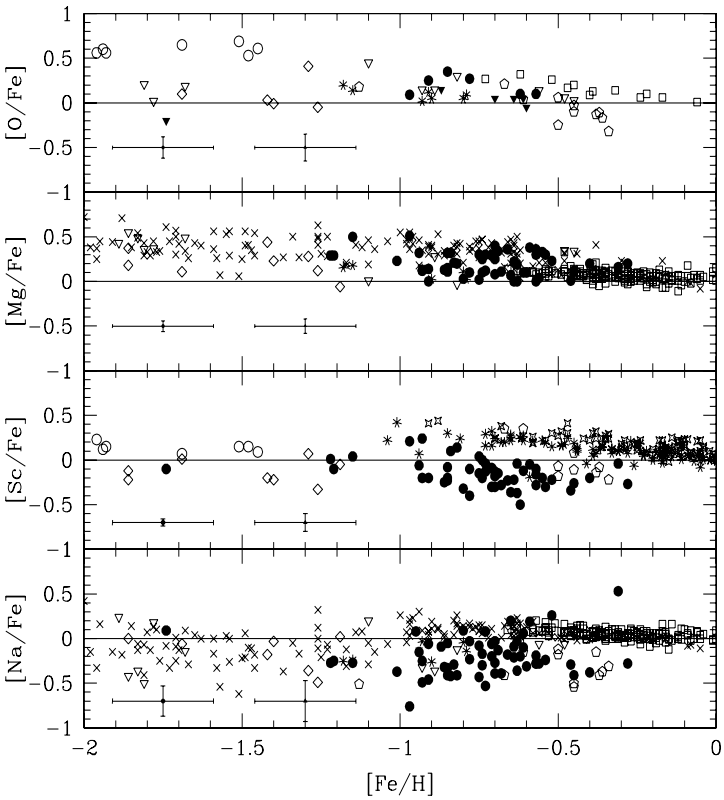

Fig. 9. Abundance distributions for the inner disk LMC stars: [O, Mg, Na, Sc/Fe] vs. [Fe/H] (symbols are the same as in Fig. 8, and we added: open stars – Allende Prieto et al. 2004; crosses – Bensby et al. 2004, only for oxygen; asterisks – Nissen et al. 2000, for Sc; Nissen & Schuster 1997, for the other elements).

of the Galaxy, but with lower mean values. In contrast, Na and Sc behaviors are similar to those of the α-elements Ti and Si. Both elements are deficient and show lower values for higher metallicities, while for the metal-poor tail, a match to the Galactic samples is observed. From this figure we see that the different LMC samples agree very well for all elements, Mg, O, Na, and Sc, even the LMC globular clusters of H00, H04 and JIS06. A few stars in the NS00 sample of low-α stars show low [Sc/Fe] ratios and overlap our sample, but most of them show solar [Sc/Fe] values, higher than in our LMC sample. Sodium abundances in NS97 sample are similar to our values, although with a higher mean abundance. It is important to notice that sodium abundances in giants are still uncertain. Pasquini et al. (2004) find that [Na/Fe] ratios in giant stars are slightly higher than those from dwarf stars in the same cluster. High [Na/Fe] ratios are also inferred from giants in M 67 (Tautvaišiene et al. 2000). But such results have not been confirmed in the reanalysis of [Na/Fe] in giants and dwarfs of M 67 (Randich et al. 2006).

Nissen et al. (2000) also found that Sc behaves similarly to Na, showing lower [Sc/Fe] ratios in their low-α stars, suggesting a correlation among those elements. To test the hypothesis of a correlation among Na and α-elements and Sc and α-elements we applied a statistical test to check for the existence and significance of such correlation, calculating the linear correlation coeficient, which varies from 1 or −1 (maximum correlation or anti-correlation) to 0 (no correlation). We have found that the correlations are weak: for Na-Ca, a correlation coefficient $\phi = -0.06$ is found, and for Sc-Ca, $\phi = 0.39$.

5.3. Iron-peak elements

Abundance distributions for the iron-peak elements are shown in Fig. 10. The iron-peak elements Co, Ni, and Cr display a very distinct pattern in the LMC inner disk stars, with underabundant values compared to the Galactic distributions and many subsolar ratios. [Co/Fe], [Cr/Fe] and [Ni/Fe] show a flat trend for most of the metallicity range, with mean abundances of ∼−0.18 dex for Cr, ∼−0.24 for Ni, and ∼−0.14 dex for Co. The [V/Fe] ratios are similar to the galactic halo and disk patterns and track the solar value, with a group of stars showing lower values. Results from the LMC GC of JIS06 seem to agree with our samples for Co, Ni, and Cr. Vanadium in their sample shows an offset, with abundance ratios corresponding to the stars with lower values in our sample. NS97 low-α stars overlap our sample for Ni and Cr, but lie in the high abundance envelope of the distributions.

According to nucleosynthetic predictions, iron-peak elements are mainly produced in SNe Ia (Iwamoto 1999; Travaglio et al. 2005): while each SN Ia produces ≈0.8 $M_\odot$ of the solar iron-peak elements, SN II produce ≈0.1 $M_\odot$ each (Timmes et al. 2003). The difference in the distributions from one environment to the other are evidence that the production factors for each iron-peak element are not the same in the different types of SNe and depend on the SFH of the parent population. This will be further discussed in Sect. 7.

5.4. Copper

In Fig. 11 we show the plot for Cu. We have found that in the inner disk LMC stars, the copper distribution is flat, with a mean value of [Cu/Fe] = −0.68 dex. Comparing it to the Galaxy, there is an overlap between the LMC and halo stars at the metal-poor end ([Fe/H] < −1.3 dex); for the higher metallicity range, the distributions diverge, with LMC stars showing a clear underabundance with respect to the Galactic disk. JIS06 also found an offset in their [Cu/Fe], compatible to our abundance ratios.

Although originally associated with the iron-peak elements, the origin of copper is still much-debated (e.g. Bisterzo et al. 2004; Cunha et al. 2004; Mishenina et al. 2002). Sometimes its main source is attributed to SNe Ia (Matteucci et al. 1993;

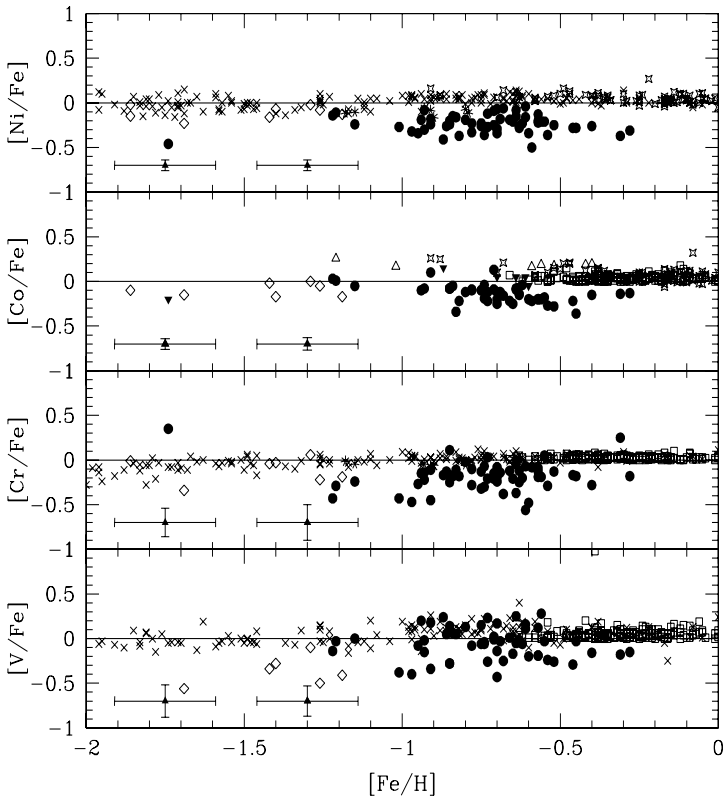

Fig. 10. Abundance distributions for the inner disk LMC stars: [iron-peak/Fe] vs. [Fe/H] (symbols are the same as in Figs. 8 and 9, and the solid downtriangles depict upper limits for our sample stars).

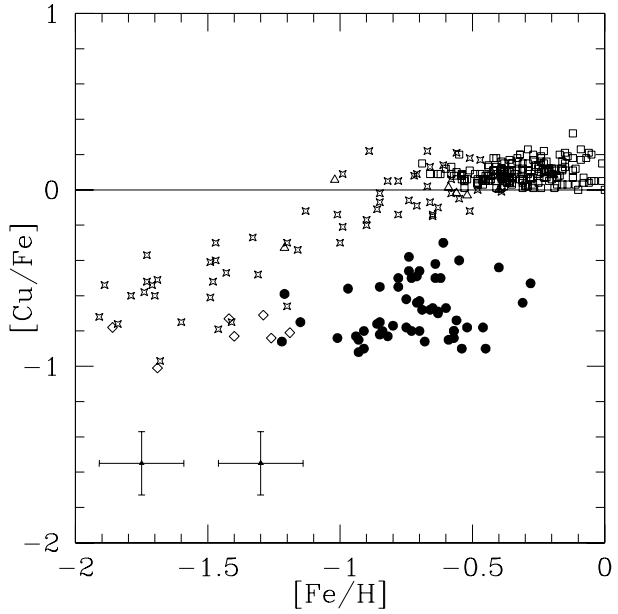

Fig. 11. Abundance distributions for inner disk LMC stars: Copper. The symbols are the data from: our sample stars (dots); Mishenina et al. (2002, stars), Prochaska et al. (2002, open triangles), Reddy et al. (2003, open squares), Johnson et al. (2006, diamonds).

Cunha et al. 2002; Mishenina et al. 2002) and sometimes to SNe II, particularly to a metallicity-dependent mechanism (Bisterzo et al. 2004; McWilliam & Smecker-Hane 2005). If the elemental behavior of the present sample, with low [α/Fe], low [iron-peak/Fe] ratios, is due to a higher contribution from SNe Ia, the overall low [Cu/Fe] pattern indicates that thermonuclear supernovae cannot be the main source of Cu production.

5.5. *s*-process elements

We find interesting elemental distributions for the *s*-process elements for our sample stars (Fig. 12). While the light *s*-process elements (hereafter *ls*: elements made by the *s*-process with atomic number lower than ~45) Zr and Y, show subsolar ratios with mean abundances the heavy *s*-process elements (hereafter *hs*: elements made by the *s*-process with atomic number higher than ~50), La and Ba show supersolar values with enhanced pattern compared to those of the Galaxy. The underabundance of *ls* elements is quite strong, [Y/Fe] = −0.33 dex and [Zr/Fe] = −0.48 dex, and Zr shows a hint of decreasing with increasing metallicities. Of the *hs* elements, Ba has a peculiar behavior with a high value for one metal-poor star ([Fe/H] < −1.4 dex), mild enhancements until [Fe/H] ~ −1.15 dex, increasing again towards higher metallicities. Lanthanium shows no trend with metallicity, with mild enhancements everywhere. One star, RGB_1118, has particularly high La and Ba abundances ([Ba/Fe] and [La/Fe] ≥ +1.0 dex) and could be a star enriched in *s*-process elements (via mass-transfer from a former AGB companion), although it is not possible from our present data to distinguish between enhancements of *s*-process or *r*-process elements. The *s*-process elements in JIS06 sample are different when compared to our results. While they find no offset for the *ls* elements compared to the galactic distribution, therefore showing a higher abundance compared to our stars, their *hs* elements (Ba and La) are less enhanced than ours. Comparing NS97 low-α stars with our sample, we find that these stars show abundances nearer those of normal disk stars for Ba and Y than the LMC stars.

The *hs*/*ls* ratios are high, showing large scatter, with a mean value of [*hs*/*ls*] = +0.77 dex, as can be seen in Fig. 13. This is very different from what is observed for the Galactic halo and disk stars, which fall around −0.2 to +0.2 dex (e.g.

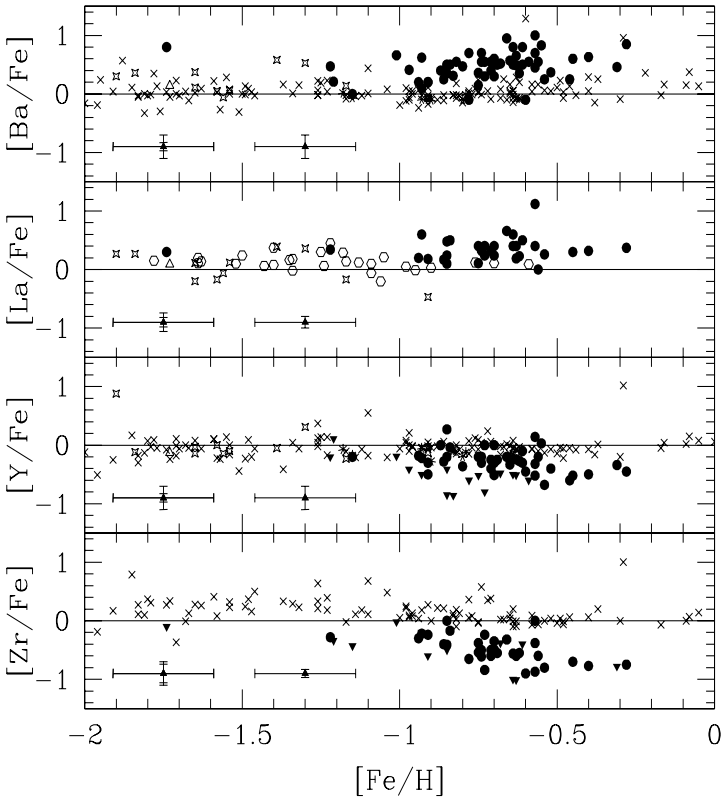

Fig. 12. Abundance distributions for inner disk LMC stars: [*s*-elements/Fe] vs. [Fe/H]. The large dots (or downtriangles for upper limits) depict our sample stars, while open symbols represent galactic samples: symbols as in Fig. 8, plus Burris et al. (2000, stars), Johnson & Bolte (2002, open trianlges), Simmerer et al. (2004, open hexagons).

Pagel & Tautvaišiene 1997; Travaglio et al. 2004). A slowly, increasing trend with metallicity is observed.

High abundances of elements heavier than Zr were also derived for LMC and SMC supergiants (Russell & Bessell 1989; Spite et al. 1993; Hill et al. 1995). Hill et al. (1995) for example, found that the light *s*-elements Zr and Y show solar composition in LMC supergiants, while heavier *s*-elements (Ba, La, Nd), as well as the *r*-process element Eu, are enhanced by +0.30 dex. As discussed by these authors, the overabundance of the heavier *s*-process and *r*-process elements seems to be a characteristic of the Magellanic Clouds and indicates a particular evolution of that Galactic system, although no satisfactory explanation is proposed for it.

To evaluate the *r*-process and *s*-process contributions within our sample, we analyzed the *r*-process content of one of our sample stars for which we have UVES spectra that cover the Eu λ 6645 Å line. The Eu and Ba abundances were derived from these spectra in the same way as for GIRAFFE spectra. For RGB_666 we find [Ba/Fe] = +0.52, and [Eu/Fe] = +0.40 dex. The corresponding [Ba/Eu] ratio of 0.12 (to be compared with the solar *r*-process [Ba/Eu] = −0.55 and the solar *s*-process [Ba/Fe] = +1.55, following Arlandini et al. 1999) indicate that this star contains a significant *r*-process contribution at a value close to the solar *s*/*r* mix at intermediate metallicities (RGB_666: [Fe/H] = −1.10).

A high content of *r*-process elements seems to contradict the observed low [α/Fe] ratios (both produced in massive stars). More data on Eu abundances are needed to confirm this high content of *r*-process elements and, in particular, the trend of the *s*/*r* fraction (traced by [Ba/Eu]) as a function of metallicity will help to constrain the source of the high content of heavy *s*-process elements in the LMC disk. We intend to tackle this issue in the two other fields (bar and outer disk) of our LMC program, since one of the MEDUSA wavelength ranges covers the Eu line for these fields.

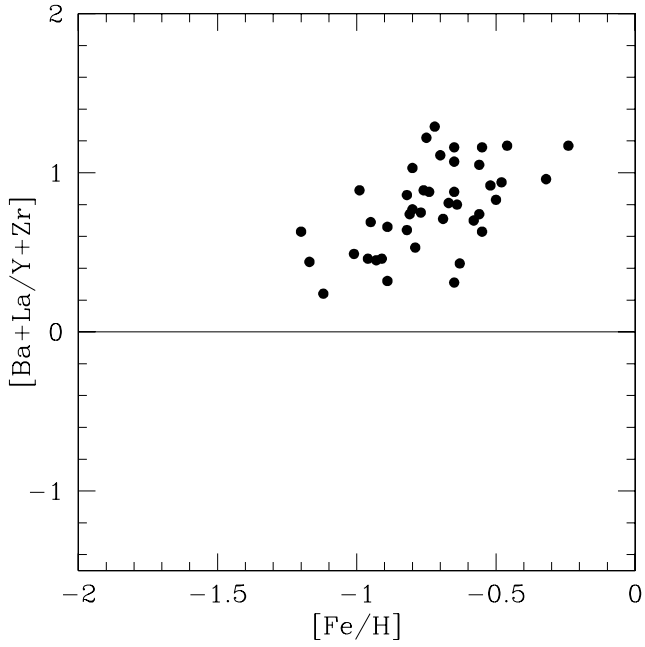

Fig. 13. Observed abundance ratios [*hs*/*ls*] = [Ba+La/Y+Zr].

5.5.1. The NaMg, NaNi relations

In the paper by NS97, the authors find a correlation between Na and Ni for their halo stars (both "normal" and "low-α" stars). Such a correlation has been confirmed for a group of stars in the dwarf spheroidal galaxies (Shetrone et al. 2003, SH03; Tolstoy et al. 2003, TO03; Venn et al. 2004). To evaluate this trend, we plot the [Ni/Fe] vs. [Na/Fe] relation for our sample stars (dots) in Fig. 14, together with NS97 low-α stars. We see that the LMC stars also show a correlation between Na and Ni, although with

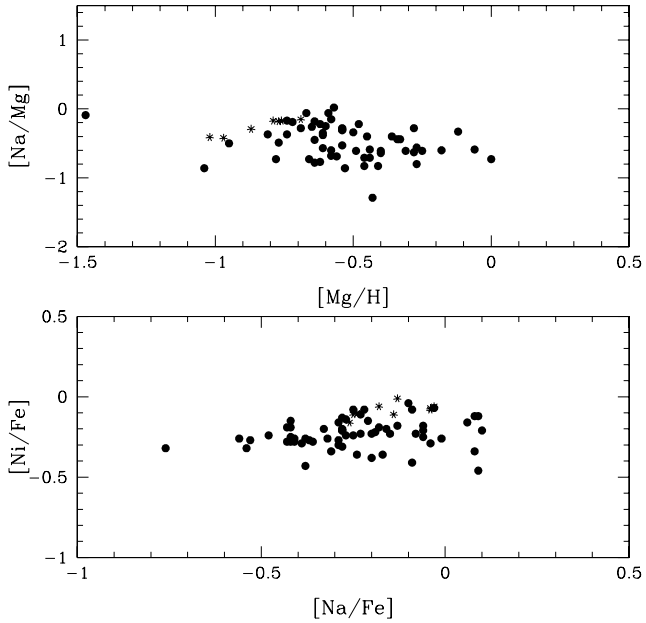

Fig. 14. The NaNi and NaMg abundance relations. Our sample stars are depicted as dots and NS97 low-α stars as starred symbols.

a flatter pattern than the increasing trend observed for the NS97 sample. According to Tsujimoto et al. (1995), Ni can be produced in SNe Ia without Na production; therefore, a higher contribution from SNe Ia would flatten the NaNi relation[3] (Venn et al. 2004) and could explain the behavior of the LMC stars. In Fig. 14 we also analyze the correlation between Na and Mg and find decreasing [Na/Mg] ratios for increasing [Mg/H] ratios. The NS97 low-α stars seem a continuation of the observed trend.

6. Comparison to the dwarf spheroidal galaxies

In Figs. 15 and 16 we compare the chemical distributions of our LMC sample to those of the dSph galaxies of Shetrone et al. (2003) and Tolstoy et al. (2003), and the Sagittarius dwarf galaxy (Sgr) of Bonifacio et al. (2004) and Sbordone et al. (2007). The elemental distributions of most dSph galaxies are more concentrated in the metallicity range for which we have the lowest number of stars, [Fe/H] < -1.2, so the present analysis is not ideal. In Fig. 15 the distributions for the α-elements Ca, Ti, and Si and for Cu are depicted (the description of the different symbols are given in the figure captions). As can be seen from these figures and also observed for O, Mg, Na, and Sc, there is an overlap among the LMC abundance ratios and those of the dSph galaxies. The same occurs for the iron-peak elements Cr, V, and Ni and for Cu (with the exception of Fornax, which shows higher values for Cu). In particular, the agreement among our data and those of the Sagittarius dwarf galaxy is very good, except that this galaxy shows [Ti/Fe] and [Mg/Fe] ratios to be slightly underabundant relative to our values.

For the *s*-process elements, depicted in Fig. 16, the dSph galaxies show enhanced *hs* and deficient *ls* compared to the Galactic behavior, although the general pattern is less discrepant than what is shown by the LMC inner disk stars, except for Sgr, which shows striking similar ratios when compared to our data. Fornax has a more metal-rich star (Fnx21) with high *s* content, which may be an *s*-enriched star. The [Ba/Y] ratios show a large offset relative to Gsalactic samples, of the same order magnitude we found. Venn et al. (2004) attribute such an offset to primary *s*-process production by low-metallicity AGB stars.

The very similar elemental distributions of the Sgr galaxy indicate that this galaxy must have been very similar to LMC, i.e., with a higher mass content, which nowadays may be hidden in streams and/or dynamically mixed to the Galaxy.

7. Discussion

It is an amazing opportunity to have so much data on the amount of various elements of stars in an external galaxy. With this unique dataset, we can now explore the SFH in more detail and understand the evolution of the LMC disk better. The overall low [X/Fe] ratios indicate that such stars have undergone a global process which is different from what is experienced by the average halo and disk stars in the Galaxy. In this section we discuss the possible explanations for this behavior.

We have found an overall low abundance pattern for the α-elements, in agreement with many previous works on stars in this galaxy (Sect. 1). The heavy *s*-elements show an enhancement relative to the Galactic disk distributions, as inferred before for supergiants and red giants in the LMC. New results from the present work include low light-*s* abundance ratios ([Y/Fe] and [Zr/Fe]), with most of the stars showing subsolar values and an unexpected offset for the iron-peak elements Ni, Cr, and Co, and in some stars, also for V. Both Na and Sc are deficient with many subsolar ratios relative to iron, and Cu shows a very low abundance in all stars from the present sample, with mean [Cu/Fe] ~ -0.7 dex, and no trend with metallicity.

As seen in previous sections, low [α/Fe] ratios have already been observed in other stellar systems such as the chemically peculiar halo stars (NS97, NS00), the dSph galaxies of the Local Group (Shetrone 2003; Tolstoy 2003), the Sagittarius galaxy (Smecker-Hane & McWilliam 2002; Bonifacio et al. 2004; Monaco et al. 2005; Sobordone et al. 2007), as well as in samples in the LMC (e.g. Hill et al. 2000, 2003; SM02; Garnett 2000; Korn et al. 2002). It is interesting to notice that the *s*-process trends in the dSph galaxies (enhanced *hs* and deficient *ls* ratios) are the same as for our stars. Correlations between abundances of iron-peak elements and α-elements were also observed in other stellar systems. A pattern of slightly deficient Ni and Cr has been observed for the low-α stars of NS97. Bensby et al. (2003) find a correlation among the [iron-peak/Fe] and [Na/Fe] vs. [α-elements/Fe] abundance ratios, i.e., sligtly higher [Cr/Fe], [Ni/Fe] and [Na/Fe] ratios in thick disk stars with enhanced [α-element/Fe] ratios (see their Fig. 13). Sbodorne et al. (2007) found subsolar ratios for Na, Sc, Co, Ni, and V in their analysis of the Sagittarius dwarf galaxy stars, which also has low [α/Fe] ratios. Such behavior may tell us interesting details about the formation of these elements and give clues to low-mass galaxy formation.

Many interpretations have been given for the low [α/Fe] ratios observed. One hypothesis is that the SF developed slowly, in short bursts, followed by long quiescent periods without SF, during which the SNe Ia contaminated the ISM and increased the Fe content (e.g. Gilmore & Wyse 1991). Lower SNe II/SNe Ia ratios, therefore a higher frequency of SNe Ia relative to SNe II, have also been invoked, within a bursty or continuous regime and with or without galactic winds (e.g. Pagel & Tautvaišiene 1997; Smith et al. 2002). A steepened IMF relative to that of the solar neighborhood has been proposed by Tsujimoto et al. (1995) and de Freitas Pacheco (1998), whereas alpha-enriched

[3] However Travaglio et al. (2005) found that some Na and Mg are also produced in SNe Ia.

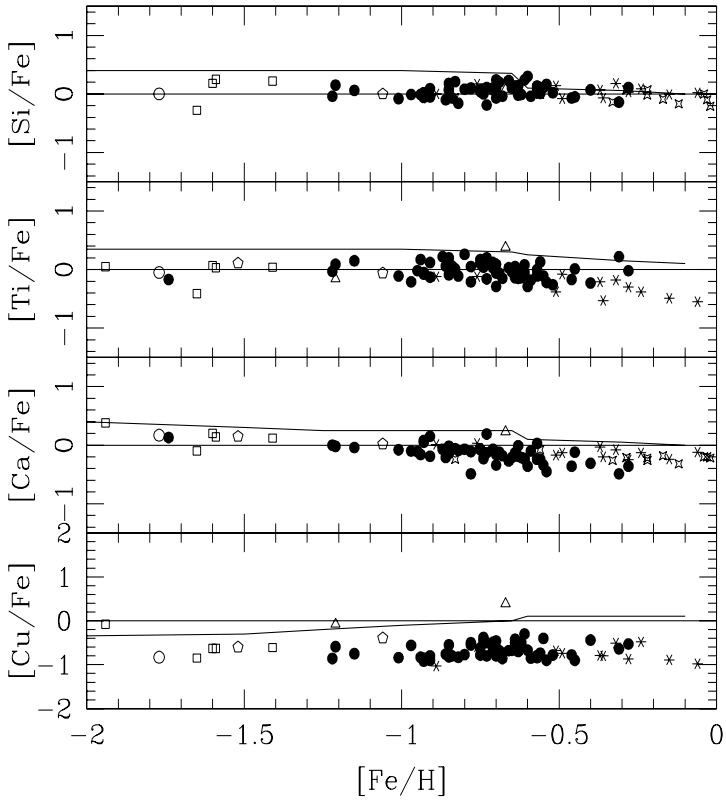

Fig. 15. Comparison of the inner disk LMC stars with stars from the dwarf spheroidal galaxies and the Sgr galaxy. 1. Alpha elements. The symbols are our sample (dots), Leo I (open pentagons), Sculptor (open dots), Fornax (open triangles), Carina (open squares), and Sgr (Bonifacio et al. 2005 – stars; Sbordone et al. 2007 – asteriks). Solid lines depict mean values of the Galactic distributions for each element.

galactic winds, which would lower the [alpha/Fe] content, have been suggested by Pilyugin (1996). Finally, a small (low-mass) SF event that would effectively truncate the IMF, yieding fewer high-mass SNe II than produced by normal SF events has been suggested (Tolstoy et al. 2003). To find explanations for the behavior of the iron-peak elements is more puzzling, since they are predicted to be produced basically in SNe Ia (e.g. Travaglio et al. 2005). A possible explanation is that the yields of the SNe Ia are dependent on metallicity (Timmes et al. 2003).

The abundance distributions observed for the *hs* and the *ls* elements, with hs/ls = [Ba+La/Y+Zr], agree with the hypothesis that the *s*-process in AGB stars is metallicity-dependent (Busso et al. 1999, and references therein; Busso et al. 2001; Abia et al. 2003; Travaglio et al. 2004). It has been noticed that, due to details of the nucleosynthesis of the *s*-process, *hs*-elements (e.g. Ba, La and Nd) tend to be produced by metal-poor AGB stars compared to *ls* elements (e.g. Y, Zr, and Sr), which are most efficiently produced at [Fe/H] ≈ -0.1 (e.g. Fig. 1 of Travaglio et al. 2004). If the SF is slow, low-metallicity AGB stars have enough time to contaminate the ISM, leaving noticeable chemical signatures for the next generations.

Nevertheless, Venn et al. (2004) discuss the possibility that the abundances of these elements (including Y) in dSph cannot be accounted for solely by the *s*-process, requiring a strong contribution from the *r*-process. Also, according to Richtler et al. (1989) and Russell & Dopita (1992), the most probable explanation for the high Ba and La abundances observed in the Magellanic Clouds is an additional *r*-process component. This would mean that *hs* and *ls* elements are produced at different rates by the *r*-process nucleosynthesis, probably in different sites. Therefore, the analysis of the behavior of the *s*-elements in the given metallicity range is complex and must take both the *r* and the *s* contributions into account.

7.1. Galaxy formation and evolution

One of the most debated themes about galaxy formation in the Universe under a ΛCDM hierarchical scenario concerns the problem of overprediction of galaxy counts at low-z and underprediction at high-z (Cimatti et al. 2002). One of the consequences for the Local Group is a larger number of small galaxies than is actually observed, although the number of dwarf galaxies observed around the Milky Way and M 31 has lately grown significantly (e.g. Belokurov et al. 2007). According to these models, numerous merging and accretion events play an important role in the formation process of massive galaxies (e.g. Moore et al. 1999), although not all dark matter clumps are predicted to host SF and thereby become visible galaxies (e.g. Bullock & Johnston 2005). The quest for signatures of possible accreted stars from nearby galaxies in the Galactic halo and disk have been carried out, without definite conclusions (NS97; NS00; Ivans et al. 2003; Venn et al. 2004). A careful inspection of the elemental distributions of the different Galactic components reveals a low dispersion in the abundance ratios at each metallicity bin and smooth transitions between them (see e.g. plots from Venn et al. 2004). This seems to indicate a different process: the Galaxy, including the halo, has grown in a holistic way, rather than by many independent accreting events, even for the Galactic halo (see Gilmore & Wyse 2004). Another possibility is that the merging events occurred very early in the building process of our Galaxy, involving mostly dark matter and primordial gas. Such observational features hint at a common history within the same environment rather than a mix of SFHs. The results from the present work strongly support this idea, showing that an LMC-like SFH results in quite a distinctive elemental pattern not seen in any galactic stellar population.

We have found that the elemental compositions of the LMC inner disk stars show a different pattern when compared to their galactic counterparts (if we exclude the low-alpha stars

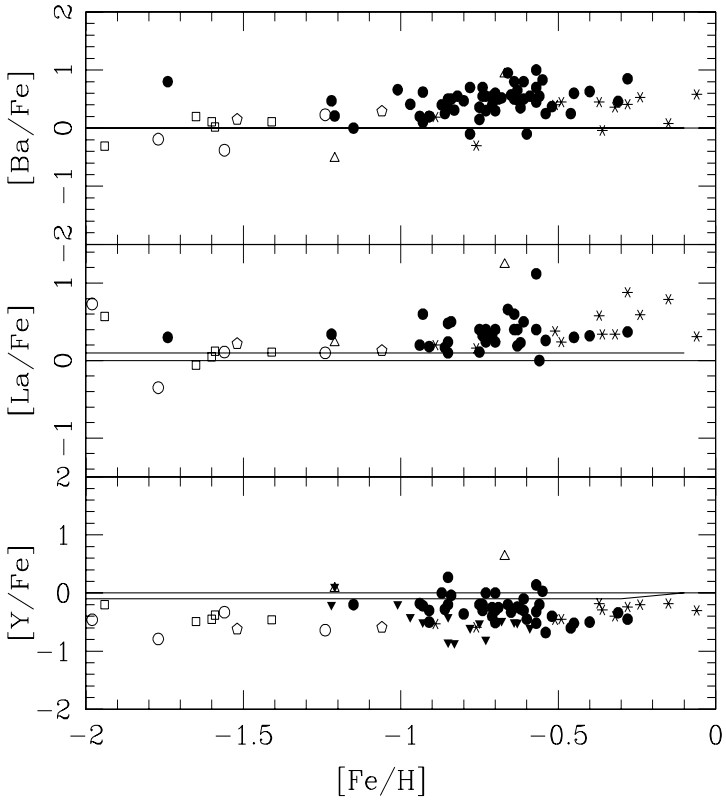

Fig. 16. Comparison of the Inner Disk LMC stars with stars from the dwarf spheroidal galaxies. 2. *s*-process elements (symbols are the same as in Fig. 15).

of NS97). This indicates that possible accreting events of LMC and LMC-like fragments (Bekki & Chiba 2005; Robertson et al. 2005), from which our Galactic halo could have been built, are unlikely, but strong conclusions are still not possible because more representative samples are needed from both halo and LMC stars. However, we stress here that the stellar populations probed in the LMC mostly have an intermediate age and would not have been merged into a Milky Way halo or disk, if the accretion of an LMC-like galaxy occurred early on ($z > 1$). Strong conclusions concerning the possible early accretion of LMC-type systems therefore still await detailed analysis of the elemental abundances of representative samples of the oldest populations in the LMC. The elemental distributions of the LMC inner disk also hint at a different process of galaxy formation, showing that the galactic local environment is fundamental for the the amount of various elements of its components.

8. Summary

In the present paper we report abundance ratios for a series of elements, including α, *s*-, and iron-peak elements, Na, Sc, and Cu for a sample of 59 RGB stars of the inner disk of the LMC. We found a very different behavior for most of the elements relative to stars from the Galaxy with similar metallicity, hinting at a very different evolutionary history. On the other hand, there is good overall agreement between the the elemental distributions of our sample stars and previous results of the LMC GC and field stars of Hill et al. (2000, 2003), Smith et al. (2002), and Johnson et al. (2006). The main results are summarized as follows:

– [α/Fe] ratios show an overall deficient pattern relative to Galactic distributions, in agreement with a slower SFH in the LMC, leading to a stronger type Ia supernovae influence. However, all α-elements do not show the same degree of deficiency: while O/Fe and Mg/Fe are hardly different in the LMC and Milky-Way disks, Si, Ca, and Ti are strongly underabundant. This illustrates that all α-elements are not alike from the nucleosynthesis point of view.
– Cu is strongly depleted with respect to iron, [Cu/Fe] $\simeq -0.70$ dex, with no apparent trend with metallicity. This also hints at a strong contribution of type Ia supernovae to the creation of copper.
– The [X/Fe] deficiency of the α-elements is also displayed by Na, Sc, and, in an unexpected behavior, by the iron-peak elements Ni, Cr, and Co. The iron peak elements underabundances are not expected in any standard chemical evolution model (i.e. currently not predicted by SNe yields).
– We have found relationships between Na-Ni and Na-Mg, in agreement with those derived by Nissen & Schuster (1997) for a sample of low-α halo stars. As Na is predicted to be mainly produced by SNe II, together with O and Mg, a relationship Na-Mg is expected, althoug Na production is also controlled by the neutron excess during carbon burning in massive stars (Umeda et al. 2000). The Na-Ni relationship is also expected if Ni is also produced in SN II, with yields dependent on the neutron excess (Thielemann et al. 1990).
– Heavy neutron capture elements fall into two well-defined groups: while high-mass *s*-process elements (Ba and La) present an enhanced pattern, low-mass *s*-process elements (Y and Zr) are deficient compared to the galactic samples. Such behavior has been observed before in LMC and SMC F supergiants and in dSph galaxy RGB stars. It could reflect a strong contribution by metal-poor AGB stars to the metal-enrichment of these systems, as low-metallicity AGB stars tend to produce the heavier *s*-process elements over the lighter ones (see Travaglio et al. 2004, for the theoretical side; and de Laverny et al. 2006, for the observation of low metallicity AGBs).
– We have derived Eu abundances for one of our intermediate-metallicity stars (RGB_666: [Fe/H] = −1.10), and combined

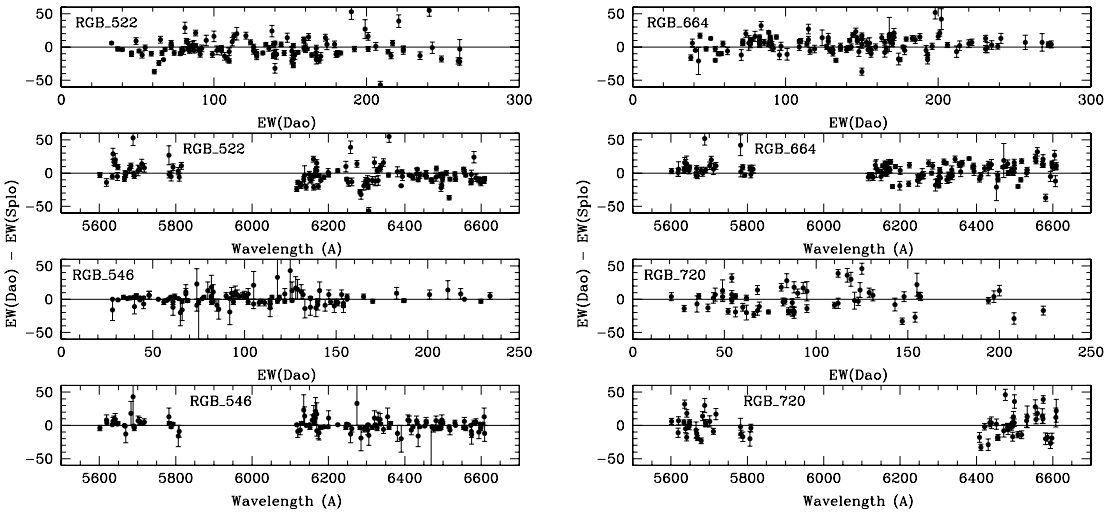

Fig. A.1. Difference between the *EW* derived using the DAOSPEC program and the Iraf task Splot: trends with respect to the *EW*(Dao) and to the wavelenght of the lines for RGB_522 and RGB_546 (*upper plot*) and for RGB_720 and RGB_664 (*lower plot*).

with the measured Ba abundance for this star, this enabled us to disantangle the respective *r*- and *s*-process contributions to heavy neutron-capture elements. This star contains a solar mix of *r*- and *s*-process elements. Although a single measurement is obviously not enough to lead to a conclusion, we thereby confirm that the high abundances of *ls* elements observed at intermediate metallicity should be attributed to the *s*-process.

For the next two fields of our program (see Introduction), the wavelength range of the spectra covers a Eu line and a better evaluation of such contributions will be possible.

– Compared to the dSph galaxies, similar abundance ratios for almost all the elements have been derived, with slight enhancements of La, Ba, Na, and Y, although the match in metallicity among our sample and the dSph samples is not ideal. The LMC inner disk abundances of Ca, Si, Ti, and Cu are also similar to those of the Sagittarius dwarf galaxy. The commonalities between the LMC inner disk population and the samples in dSph galaxies indicate that all these galaxies may have undergone similar SFH.

The overall pattern of the elemental distributions for the LMC inner disk population can be explained by a higher contribution of type Ia SNe, indicating that the build up of this population has been slower than that of the solar neighborhood stars. A bigger contribution from metal-poor ABG stars is also proposed. The present results support the hypothesis that the elemental distributions of the stars are directly related to the galaxy they belong to.

Acknowledgements. L.P. acknowledges CAPES and FAPESP fellowships #0606-03-0 and #01/14594-2. We thank Peter Stetson for the availability of the DAOSPEC program.

Appendix A: Comparison between equivalent width from DAOSPEC and from Splot-Iraf

In order to evaluate the quality of the DAOSPEC estimates, we have derived by eye inspection the *EW* of six stars, using the Splot Iraf task. We have chosen stars in a range of *S/N* ratio typical of our total sample in order to better evaluate the errors: S/N = 54 for RGB_522, 59 for RGB_546, 47 for RGB_664, 42 for RGB_666, 26 for RGB_720, and 47 for RGB_1055. The detailed values are given in Table A.1. We have found two problems relative to the DAOSPEC results from GIRAFFE spectra: a) not all blends have been identified, nevertheless all lines with weak blends (which are most of the lines) have been correctly analyzed by the iterative process of the program; b) cosmic rays also have not been identified, and those lines too near CR features must be discarded. Therefore the use of DAOSPEC requires spectra and line lists as clear as possible from blends and spectra as clean from cosmic hits as possible. As can be seen in Table A.1, we have found a very good agreement between the program results and those from the Splot manual measurements. The average difference *EW*(Dao) – *EW*(Splot) is 0.46 mÅ for the six stars, with no strong systematic trend in one direction or the other (the mean difference for each star ranges from −3.7 to +5 mÅ). However, the dispersion of the measurements around the mean are higher, between 9.4 mÅ for RGB_1055 and 22.2 mÅ for RGB_666. These dispersion seem to anticorrelate with S/N as expected (the two stars with the highest dispersion are the two lowest quality spectra), and may also correlate with temperature, although our sample of 6 stars is not quite high enough to investigate these dependancies any further.

We have checked for systematic trends on the *EW* with wavelength and with the *EW* strength by plotting the differences *EW*(Dao) – *EW*(Splot) vs. wavelength and *EW*(Dao) – *EW*(Splot) vs. *EW*(Dao) for four stars, as shown in Fig. A.1. No trends have been found and confort us in the validity of using DAOSPEC *EW* mesurement for atmospheric parameter determinations (effective temperature and microturbulence velocities).

In Table A.2 we give the differences for the abundances derived from DAOSPEC and Splot, Ab(Dao) – Ab(Splot). As can be seen in this table, the agreement between the two methods is good for most of the elements, always better than the typical errorbars given for our measurement of the corresponding elements, and usually below 0.10 dex. The differences are higher for those elements with fewer lines (e.g. Na I and Ti I), which increases the weight of the scatter among lines. Let us note in particular that elements such as Ca I or Ti I do not seem to be affected by the method used for *EW* measurement in a systematic direction, so that the strong underabundances found for these elements (with respect to the galactic trends) are robust against *EW* systematics.

Table A.2. Absolute differences Ab(Dao) – Ab(Splot) and the average value (see text).

Element	RGB_522	RGB_546	RGB_664	RGB_666	RGB_720	RGB_1055	Average difference
CA1	–0.03	0.13	–0.04	0.03	–0.06	–0.09	–0.01 ± 0.08
CR1	–0.08	0.03	0.10	–0.05	–0.05	0.11	0.01 ± 0.08
FE1	–0.11	0.01	0.10	–0.01	–0.06	0.00	–0.02 ± 0.07
FE2	–0.13	–0.06	–0.02	0.04	–0.05	–0.10	–0.05 ± 0.06
NA1	0.08	0.09	0.18	–0.06	0.06	–0.06	0.05 ± 0.09
NI1	–0.03	–0.06	0.09	0.04	–0.12	–0.09	–0.03 ± 0.08
SI1	–0.05	0.01	–0.01	0.07	0.20	–0.03	0.03 ± 0.09
TI1	–0.06	0.00	0.14	0.02	–0.16	–0.10	–0.03 ± 0.10
TI2	–0.18	–0.07	0.13	0.0	0.13	0.06	0.01 ± 0.12
V1	–0.05	0.02	0.10	–0.22	–0.10	–0.09	–0.06 ± 0.11

References

Abia, C., Domínguez, I., Gallino, R., et al. 2002, ApJ 579, 817
Allende Prieto, C., Barklem, P. S., Lambert, D. L., & Cunha, K. 2004, A&A, 420, 183
Allende Prieto, C., Lambert, D. L., & Asplund, M. 2001, ApJ, 566, L63
Barbuy, B., Zoccali, M., Ortolani, S., et al. 2006, A&A, 449, 349
Belokurov, V., Zucker, D. B., Evans, N. W., et al. 2007, ApJ, 654, 897
Bensby, T., Feltzing, S., & Lundstrom, I. 2003, A&A, 410, 527
Bensby, T., Feltzing, S., & Lundstrom, I. 2004, A&A, 415, 155
Bessell, M. S. 1991, A&A, 242L, 17
Bessell, M. S., Castelli, F., & Plez, B. 1998, A&A, 333, 231
Biehl, D. 1976, Ph.D. Thesis, Kiel
Biemont, E., Baudoux, M., Kurucz, R. L., Ansbacher, W., & Pinnington, E. H. 1991, A&A, 249, 539
Bisterzo, S., Gallino, R., Pignatari, M., et al. 2004, MmSAI, 75, 741
Bonifacio, P., Sbordone, L., Marconi, L., Pasquini, L., & Hill, V. 2004, A&A, 414, 503
Bord, D. J., barisciano, L. P., & Cowley, C. R. 1996, MNRAS, 278, 997
Bullock, J. S., & Johnston, K. V. 2005, ApJ, 635, 931
Burris, D. L., Pilachowski, C. A., Armandroff, T. E., et al. 2000, ApJ, 544, 302
Busso, M., Gallino, R., & Wasserburg, G. J. 1999, ARA&A, 37, 239
Busso, M., Gallino, R., Lambert, D. L., Travaglio, C., & Smith, V. V. 2001, ApJ, 557, 802
Butcher, H. 1977, ApJ, 216, 372
Carpenter, J. M. 2001, AJ, 121, 2851
Cayrel, R. 1988, in The Impact of Very High S/N Spectroscopy on Stellar Physics, ed. G. Cayrel de Strobel, & M. Spite (Dordrecht: Kluwer), IAU Symp., 132, 345
Cayrel, R., Depagne, E., Spite, M., et al. 2004, A&A, 416, 1117
Cimatti, A., Pozzetti, L., Mignoli, M., et al. 2002, A&A, 391, L1
Cioni, M.-R., Girardi, L., Marigo, P., & Habing, H. J. 2006, A&A, 448, 77
Cunha, K., Smith, V. V., Suntzeff, N. B., et al. 2004, AJ, 124, 379
Da Costa, G. S. 1991, in The Magellanic Clouds, ed. R. Haynes, & D. Milne (Dordrecht: Kluwer), IAU Symp., 148, 183
Da Costa, G. S. 1999, in New Views on the Magellanic Clouds, ed. Y.-H. Chu, N. Suntzeff, J. Hesser, & D. Bohlender (San Francisco: ASP), IAU Symp., 190, 397
de Laverny, P., Abia, C., Dominguez, I., et al. 2006, A&A, 446, 1107
D'Onghia, E., & Lake, G. 2004, ApJ, 612, 628
Dufton, P. L., Smartt, S. J., Lee, J. K., et al. 2006, A&A, 457, 265
de Freitas Pacheco, J. A. 1998, AJ, 116, 1701
de Vaucouleurs, G. 1980, PASP, 92, 576
Edvardsson, B., Andersen, J., Gustafsson, B., et al. 1993, A&A, 275, 101
Evans, C. J., Smartt, S. J., Lee, J.-K., et al. 2005, A&A, 437, 467
Fernie, J. D. 1983, PASP, 95, 782
Fulbright, J. P. 2000, AJ, 120, 1841
Garnett, D. R. 1999, in New Views of the Magellanic Clouds, ed. Y.-H. Chu, N. Suntzeff, J. Hesser, & D. Bohlender, IAU Symp., 190, 266
Geha, M. C., Holtzman, J. A., Mould, J. R., et al. 1998, AJ, 115, 1045
Gilmore, G., & Wyse, R. F. G. 1991, ApJ, 367, L55
Gilmore, G., & Wyse, R. F. G. 2004 [arXiv:astro-ph/0411714]
Grevesse, N., & Sauval, A. J. 1998, Space Sci. Rev., 85, 161
Grevesse, N., & Sauval, A. J. 2000, in Origin of Elements in the Solar System, Implications of Post-1957 Observations, Proc. of the International Symposium, ed. O. Manuel (Boston/Dordrecht: Kluwer Academic/Plenum Publishers), 261
Gustafsson, B., Bell, R. A., Eriksson, K., & Nordlund, A. 1975, A&A, 42, 407
Gustafsson, B., Edvardsson, B., Eriksson, K., et al. 2003, in Stellar Atmosphere Modeling, ed. I. Hubeny, D. Mihalas, & K. Werner, ASP Conf. Proc., 288 (ASP: San Francisco), 331
Hill, V. 2004, in Carnegie Observatories Astrophysics Series, Origin and Evolution of the Elements, ed. A. McWilliam, & M. Rauch (Cambridge: Cambridge Univ. Press), 4, 205
Hill, V., & Spite, M. 1999, in Galaxy Evolution: Connecting the Distant Universe with the Local Fossil Record, Proc. Coll. Obs. Paris-Meudon, ed. M. Spite (Dordrecht: Kluwer Academic Publishers), 469
Hill, V., Andrievsky, S., & Spite, M. 1995, A&A, 293, 347
Hill, V., Francois, P., Spite, M., Primas, F., & Spite, F. 2000, A&A, 364, L19
Holtzman, J. A., Gallagher, J. S., III, Cole, A. A., et al. 1999, AJ, 118, 2262
Hunter, I., Dufton, P. L., Smartt, S. J., et al. 2007, A&A, 466, 277
Ivans, I. I., Sneden, C., James, C. R., et al. 2003, ApJ, 592, 906
Iwamoto, K., Brachwitz, F., Nomoto, K., et al. 1999, ApJS, 125, 439
Javiel, S. C., Santiago, B. X., & Kerber, L. O. 2005, A&A, 431, 73
Johnson, J., & Bolte, M. 2002, ApJ, 579, 616
Johnson, J., Bolte, M., Hesser, J. E., & Ivans, I. I. 2004, in Carnegie Observatories Astrophysics Series, Origin and Evolution of the Elements, ed. A. McWilliam, & M. Rauch, 4, 29
Korn, A. J., Keller, S. C., Kaufer, A., et al. 2002, A&A, 385, 143
Korn, A. J., Shi J., & Gehren, T. 2003, A&A, 407, 691
Kraft, R. P. Sneden, C., Langer, G. E., & Prosser, C. F. 1992, AJ, 104, 645
Kurucz, R. L., Furenlid, I., & Brault, J. 1984, National Solar Observatory Atlas, Sunspot, New Mexico, National Solar Observatory, 1, 984
Lawler, J. E., Bonvallet, G., & Sneden, C. 2001, ApJ, 556, 452
Luck, R. E., & Lambert, D. L. 1992, ApJS, 79, 303
Madore, B. F., & Freedman, W. L. 1998, ApJ, 492, 110
Matteucci, F., Raiteri, C. M., Busson, M., Gallino, R., & Gratton, R. 1993, A&A, 272, 421
McWilliam, A. 1997, ARA&A, 35, 503
McWilliam, A. 1998, AJ, 115, 1640
McWilliam, A., & Rich, M. 1994, ApJS, 91, 949
McWilliam, A., & Smecker-Hane, T. 2005, ApJ, 622, 29
Mishenina, T. V., Kovtyukh, V. V., Soubiran, C., Travaglio, C., & Busso, M. 2002, A&A, 396, 189
Moore, B., Ghigna, S., Lake, G., et al. 1999, ApJ, 524, L19
Nave, G., Johansson, S., Learner, R. C. M., Thorne, A. P., & Brault, J. W. 1994, ApJS, 94, 221
Nissen, P. E., & Schuster, W. J. 1997, A&A, 326, 752
Nissen, P. E., Chen, Y. Q., Schuster, W. J., & Zhao, G. 2000, A&A, 353, 722
Olszewski, E. W., Suntzeff, N. B., & Mateo, M. 1996, ARA&A, 34, 511
Pagel, B. E. J., & Tautvaišiene, G. 1997, MNRAS, 288, 108
Pasquini, L., Avila, G., Blecha, A., et al. 2002, The Messenger, 110, 1
Pasquini, L., Randich, S., Zoccali, M., et al. 2004, A&A, 424, 951
Pilyugin, L. S. 1996, A&A, 310, 751
Plez, B. 2000, The Carbon Star Phenomenon, ed. R. F. Wing (Dordrecht: Kluwer Academic Publishers), Proc. IAU Symp., 177, 71
Plez, B., Brett, J. M., & Nordlund, A. 1992, A&A, 256, 551
Prochaska, J. X., Naumov, S. O., Carney, B. W., McWilliam, A., & Wolfe, A. M. 2000, AJ, 120, 2513
Randich, S., Sestito, P., Primas, F., Pallavicini, R., & Pasquini, L. 2006, A&A, 450, 557
Reddy, B. E., Tomkin, J., Lambert, D. L., & Allende Prieto, C. 2003, MNRAS, 340, 304
Richtler, T., Spite, M., & Spite, F. 1989, A&A, 225, 351
Rolleston, W. R. J., Trundle, C., & Dufton, P. L. 2002, A&A, 396, 53
Russell, S. C., & Bessell, M. S. 1989, ApJS, 70, 865
Russell, S. C., & Dopita, M. A. 1992, ApJ, 384, 508
Rutten, R. J. 1978, Sol. Phys., 56, 237
Sarajedini, A. 1998, AJ, 116, 38
Sbordone, L., Bonifacio1, P., Buonanno, R., et al. 2007, 465, 815
Shetrone, M. D., Venn, K. A., Tolstoy, E., et al. 2003, AJ, 125, 684

Smecker-Hane, T., & McWilliam, A. 2002, Proc. Symp. Cosmic Abundances as Records of Stellar Evolution and Nucleosynthesis in honor of David L. Lambert, ASP Conf. Ser., ed. T. G. barnes III, & F. N. Bash, San Francisco, 336, 221
Smecker-Hane, T. A., Cole, A. A., Gallagher, J. S. III, & Stetson, P. B. 2002, SMH02, ApJ, 566, 239
Smecker-Hane, T., Cole, A., & Mandushev, G. I. 2007, in preparation
Smith, V. V., Suntzeff, N. B., Cunha, K., et al. 2000, AJ, 119, 1239
Smith, V. V., Hinkle, K. H., Cunha, K., et al. 2002, AJ, 124, 3241
Sneden, C., Gratton, R. G., & Crocker, D. A. 1991, A&A, 246, 354
Sneden, C., McWilliam, A., Preston, G. W., et al. 1996, ApJ, 467, 819
Sousa, S. G., Santos, N. C., Israelian, G., Mayor, M., & Monteiro, M. J. P. F. G. 2006, A&A, 458, 873
Spite, M. 1967, Ann. Astrophys., 30, 21
Spite, F., Barbuy, B., & Spite, M. 1993, A&A, 272, 116
Subramaniam, A. 2004, A&A, 425, 837
Tautvaišiene, G., Edvardsson, B., Tuominen, I., & Ilyin, I. 2000, A&A, 360, 499
Thielemann, F.-K., Hashimoto, M., & Nomoto, K. 1990, ApJ, 349, 222
Thielemann, F.-K., Brachwitz, F., Freiburghaus, C., et al. 2001, PPNP, 46, 5
Thielemann, F.-K., Argast, D., Brachwitz, F., et al. 2002, Ap&SS, 281, 25
Timmes, F. X., Brown, E. F., & Truran, J. W. 2003, ApJ, 590, L83
Tolstoy, E., Venn, K. A., Shetrone, M. D., et al. 2003, AJ, 125, 707
Travaglio, C., Gallino, R., Arnone, E., et al. 2004, ApJ, 601, 864
Travaglio, C., Hillebrandt, W., Reinecke, M., & Thielemann, F.-K. 2005, ApJ, 425, 1029
Tsujimoto, T., Nomoto, K., Yoshii, Y., et al. 1995, MNRAS, 277, 945
Umeda, H., Nomoto, K., & Nakamura, T. 2000, in The First Stars, ed. A. Weiss, T. Abel, & V. Hill (Heidelberg: Springer), 150
van den Bergh, S. 1979, ApJ, 230, 95
van den Bergh, S. 1998, ApJ, 507, L39
van den Bergh, S. 1999, New Views of the Magellanic Clouds, ed. Y.-H. Chu, N. Suntzeff, J. Hesser, & D. Bohlender, IAU Simp., 190
van der Marel, R. P., & Cioni, M.-R. L. 2001, AJ, 122, 1807
Venn, K. A., Irwin, M., Shetrone, M. D., et al. 2004, AJ, 128, 1177
Westerlund, B. E. 1997, The Magellanic Clouds (Cambridge: Cambridge Univ. Press)
Woosley, S. E., & Weaver, T. A. 1995, ApJS, 101, 181

Table A.1. Comparison of the equivalent widths derived from DAOSPEC and Iraf-Splot task for six of our sample stars.

		RGB_522		RGB_546		RGB_664		RGB_666		RGB_720		RGB_1055	
Line	Element	Dao	Splot	Dao	Splot	Dao	Splot	Dao	Splot	Dao	Splot	Dao	Splot
6300.31	O1	–	–	–	–	96	108	–	–	–	–	–	–
6274.66	V1	173	159	118	85	171	156	–	–	–	–	75	54
6285.17	V1	140	172	92	111	170	159	71	61	–	–	61	–
6199.19	V1	206	205	126	128	193	212	90	186	–	–	79	72
6292.82	V1	167	186	111	116	174	192	70	90	–	–	–	–
6224.51	V1	134	130	77	76	147	135	44	54	–	–	32	24
6251.82	V1	170	184	119	118	165	173	69	24	–	–	–	–
6150.15	V1	167	169	92	91	178	183	44	44	–	–	54	53
6135.37	V1	146	155	74	51	150	138	47	51	–	–	40	–
6119.53	V1	139	153	85	94	136	139	63	96	–	–	65	89
6452.32	V1	103	106	43	44	43	64	21	32	44	42	–	–
6531.41	V1	105	106	41	37	109	109	–	–	45	38	–	–
6357.29	V1	37	40	–	–	–	–	–	–	–	–	–	–
6222.58	Y1	–	–	–	–	38	54	–	–	–	–	–	–
6435.01	Y1	78	88	28	44	77	67	22	47	21	17	–	–
6613.73	Y2	–	–	–	–	–	–	–	–	94	–	–	–
6496.90	BA2	249	267	218	210	239	238	209	206	200	187	–	–
6141.73	BA2	260	281	220	220	272	268	201	207	–	–	–	–
6572.80	CA1	216	229	156	156	231	218	125	145	124	110	107	120
6162.19	CA1	308	334	234	229	312	319	211	215	–	–	198	194
6169.56	CA1	179	175	140	148	188	173	143	167	–	–	134	142
6169.04	CA1	162	147	128	111	163	138	119	137	–	–	106	99
5601.29	CA1	201	204	150	154	206	203	125	129	156	150	117	129
6493.79	CA1	192	195	165	161	196	195	117	107	148	144	130	125
6166.44	CA1	144	140	105	84	143	143	98	99	–	–	104	111
6499.65	CA1	159	161	115	112	153	146	114	116	117	81	101	106
6161.30	CA1	151	172	129	114	165	158	75	55	–	–	81	88
6455.61	CA1	126	126	94	88	119	122	85	74	74	93	76	76
6439.08	CA1	224	227	187	189	241	228	182	163	197	193	163	163
6471.67	CA1	164	176	140	142	168	149	117	116	143	151	122	134
6508.84	CA1	72	72	–	–	54	74	–	–	28	42	–	–
6282.60	CO1	152	180	109	112	177	177	–	–	–	–	55	22
6117.00	CO1	–	–	–	–	–	–	–	–	–	–	29	18
5647.24	CO1	80	85	45	43	77	73	36	39	54	56	31	29
6330.10	CR1	141	152	95	85	148	155	75	44	–	–	69	74
6362.88	CR1	–	–	101	98	168	153	64	29	–	–	66	55
5787.93	CR1	102	107	69	71	110	101	39	–	68	85	47	51
5783.07	CR1	92	94	60	57	90	88	25	–	41	54	32	–
5782.13	CU1	199	172	126	113	202	160	100	98	121	123	–	–
6358.69	FE1	241	186	170	173	214	212	119	–	–	–	164	–
6498.95	FE1	183	192	156	152	200	184	137	134	157	153	126	131
6574.25	FE1	160	162	144	153	171	150	112	108	129	119	107	115
6581.22	FE1	138	114	97	93	150	187	92	110	88	108	75	72
6430.86	FE1	243	244	201	194	257	250	195	203	208	237	164	155
6151.62	FE1	140	149	118	121	136	135	100	13	–	–	92	98
6335.34	FE1	217	211	183	174	220	215	170	158	–	–	148	144
6297.80	FE1	180	191	147	151	193	205	137	160	–	–	123	117
6173.34	FE1	169	189	149	159	170	165	135	146	–	–	124	126
6421.35	FE1	214	221	187	189	222	215	200	197	194	196	157	159
6481.88	FE1	151	157	132	125	163	149	126	128	123	126	108	102
6392.54	FE1	88	86	–	–	90	79	32	26	–	–	–	–
6392.54	FE1	88	86	–	–	90	79	32	26	–	–	–	–
6608.04	FE1	99	110	80	67	128	119	32	32	95	83	–	–
6494.99	FE1	261	283	229	232	274	270	222	220	224	241	174	183
6393.61	FE1	224	229	–	–	235	232	188	–	–	–	167	161
6344.16	FE1	201	185	154	160	201	180	115	127	–	–	–	–
6593.87	FE1	181	191	154	164	192	197	141	177	154	181	120	117
5701.56	FE1	174	170	146	139	185	174	140	142	131	125	130	122
6609.12	FE1	155	163	136	148	168	157	87	94	155	133	122	108
6475.63	FE1	134	132	108	113	142	132	97	94	125	79	89	94
6137.70	FE1	261	264	211	197	268	261	200	218	–	–	174	168
6322.69	FE1	153	165	136	135	156	166	135	174	–	–	116	108

Table A.1. continued.

		RGB_522		RGB_546		RGB_664		RGB_666		RGB_720		RGB_1055	
Line	Element	Dao	Splot	Dao	Splot	Dao	Splot	Dao	Splot	Dao	Splot	Dao	Splot
6575.04	FE1	167	179	133	147	179	167	137	161	112	73	102	107
6200.32	FE1	160	162	131	120	150	146	121	129	–	–	128	120
6180.21	FE1	141	152	114	117	133	153	94	133	–	–	94	106
6518.37	FE1	132	141	114	121	144	126	112	125	95	109	93	84
6355.04	FE1	–	–	141	128	183	170	130	102	–	–	127	117
6411.66	FE1	161	164	153	146	156	160	137	136	147	180	118	118
6301.51	FE1	152	165	–	–	175	194	150	144	–	–	109	106
6302.50	FE1	128	138	105	112	129	134	87	110	–	–	89	87
6336.83	FE1	159	149	136	134	154	158	138	139	–	–	125	85
6408.03	FE1	–	–	122	114	131	140	118	117	87	105	111	106
5809.22	FE1	105	111	74	83	92	94	60	63	82	86	62	51
6188.02	FE1	84	90	69	71	90	80	57	58	–	–	51	42
6157.73	FE1	126	132	102	94	141	142	93	94	–	–	86	88
6165.36	FE1	79	83	68	57	72	67	77	104	–	–	42	58
6380.75	FE1	87	85	61	73	89	67	66	12	–	–	–	–
6380.75	FE1	87	85	61	73	89	67	66	12	–	–	–	–
5618.63	FE1	107	121	68	60	97	96	61	65	69	80	60	56
5638.27	FE1	121	104	96	89	128	114	96	90	87	92	82	70
5635.82	FE1	81	52	48	42	80	64	45	47	54	22	40	–
5641.45	FE1	115	95	93	84	–	–	77	75	81	63	69	63
5814.81	FE1	65	54	–	–	39	33	–	–	–	–	25	–
5717.83	FE1	112	104	90	85	115	104	77	70	93	76	67	66
5705.47	FE1	72	66	48	42	74	54	33	31	–	–	38	38
5691.50	FE1	90	94	56	60	79	73	36	35	62	60	43	41
5619.61	FE1	–	–	41	37	76	70	44	34	54	47	29	23
5806.73	FE1	86	83	66	82	83	75	50	–	62	82	45	46
5679.02	FE1	83	77	–	–	83	79	59	54	66	89	52	46
6597.56	FE1	53	65	37	35	83	68	40	32	56	75	37	27
6469.19	FE1	128	138	75	213	109	100	62	70	92	200	55	58
5633.95	FE1	87	92	64	63	83	78	57	58	56	51	52	46
6516.08	FE2	61	98	57	59	58	68	–	–	–	–	60	64
6432.68	FE2	33	27	40	37	51	38	47	51	53	56	–	–
6149.25	FE2	–	–	–	–	–	–	31	54	–	–	–	–
6247.56	FE2	46	55	43	41	41	46	57	50	–	–	38	53
6456.39	FE2	51	57	62	58	56	66	71	55	52	70	64	63
6320.43	LA2	100	84	83	72	90	75	40	–	–	–	–	–
6390.48	LA2	67	86	65	85	72	63	43	72	–	–	–	–
6390.48	LA2	67	86	65	85	72	63	43	72	–	–	–	–
5711.09	MG1	148	134	119	116	155	149	116	116	110	119	104	103
5688.22	NA1	190	137	125	82	198	146	100	76	119	89	37	–
5682.65	NA1	159	148	82	64	159	159	57	68	68	54	45	45
6160.75	NA1	88	67	–	–	94	79	32	42	–	–	–	–
6154.23	NA1	59	69	–	–	78	67	24	20	–	–	–	–
6327.60	NI1	139	135	102	106	131	135	84	110	–	–	73	71
6128.98	NI1	109	127	78	75	116	122	68	70	–	–	60	56
6314.67	NI1	139	150	122	125	150	133	116	165	–	–	100	91
6482.81	NI1	124	117	94	98	127	127	89	88	112	118	77	77
6532.89	NI1	74	83	53	53	89	84	33	36	49	36	–	–
6586.32	NI1	110	117	99	94	–	–	105	125	88	106	82	96
6175.37	NI1	68	72	40	51	44	27	36	57	–	–	–	–
6305.67	SC1	209	266	86	101	212	219	58	60	–	–	29	28
6604.60	SC2	91	102	82	80	115	88	31	48	125	–	60	53
5640.99	SC2	113	97	82	77	124	110	85	79	85	103	72	68
5669.04	SC2	136	138	114	127	140	144	93	96	85	104	82	87
5667.15	SC2	84	85	58	59	86	79	69	53	60	72	54	51
6245.62	SC2	95	85	66	69	101	112	76	101	–	–	57	64
5665.56	SI1	66	75	28	28	54	57	32	41	35	42	31	16
5690.43	SI1	55	56	31	32	59	54	29	–	49	45	36	39
5793.07	SI1	49	40	38	36	48	51	39	39	–	–	25	30
6599.11	TI1	128	142	82	86	147	138	–	–	–	–	34	44

Table A.1. continued.

		RGB_522		RGB_546		RGB_664		RGB_666		RGB_720		RGB_1055	
Line	Element	Dao	Splot	Dao	Splot	Dao	Splot	Dao	Splot	Dao	Splot	Dao	Splot
6126.22	TI1	152	170	114	121	166	170	81	130	–	–	72	92
6261.11	TI1	235	248	151	156	231	234	75	120	–	–	103	104
6554.24	TI1	140	134	83	86	146	123	68	66	84	56	61	64
6303.77	TI1	110	131	59	58	114	109	50	–	–	–	–	–
6258.10	TI1	221	182	139	152	232	233	114	–	–	–	108	110
6556.08	TI1	152	150	100	94	169	151	83	71	90	81	64	58
5648.58	TI1	82	73	34	31	77	68	–	–	36	31	23	18
6559.59	TI2	83	86	61	65	84	52	60	49	88	70	57	48
6491.56	TI2	103	107	75	79	91	87	67	81	83	86	59	63
6606.95	TI2	46	57	–	–	71	83	–	–	–	–	–	–